

1 Processing Multiple GNSS RO Data Using FSI and ROPP: Results from the ROMEX

2
3 Yong Chen¹, Xinjia Zhou², Xin Jing³, Shu-Peng Ho¹, Xi Shao³, and Tung-Chang Liu³

4 ¹NOAA/NESDIS/STAR, College Park, MD, 20740, USA

5 ²ERT, Laurel, MD, 20707, USA

6 ³CISESS/ESSIC, University of Maryland, College Park, MD, 20740, USA

7 Corresponding to: Yong Chen (Yong.Chen@noaa.gov)

8 9 Abstract

10
11 Global Navigation Satellite System (GNSS) Radio Occultation (RO) is a vital technique in
12 atmospheric remote sensing, providing all-weather, high-resolution vertical observations that
13 support numerical weather prediction (NWP) and atmospheric research. To enhance
14 understanding of GNSS RO processing uncertainties and inter-algorithm consistency,
15 NOAA/STAR developed an independent RO inversion algorithm based on the Full Spectrum
16 Inversion (FSI) technique to derive bending angle and refractivity profiles from excess phase
17 data. As part of the international Radio Occultation Modeling Experiment (ROMEX), endorsed
18 by the International Radio Occultation Working Group (IROWG), STAR's FSI results were
19 systematically compared with outputs from the community standard Radio Occultation
20 Processing Package (ROPP) and EUMETSAT datasets. Leveraging multi-GNSS RO
21 observations from both commercial and government-funded missions, the study evaluates
22 consistency across processing approaches using the European Centre for Medium-Range
23 Weather Forecasts (ECMWF) Reanalysis v5 (ERA5) as the reference and structural differences
24 against the three-dataset mean for the ROMEX period. Results reveal high overall agreement,
25 while identifying variations linked to the signal-to-noise ratio (SNR) and mission
26 characteristics, providing critical insights for interpreting ROMEX forecast impact studies and
27 improving GNSS RO data assimilation systems.

28 29 1. Introduction

30
31 Global Navigation Satellite System (GNSS) Radio Occultation (RO) has become a cornerstone
32 of atmospheric remote sensing, offering high vertical resolution, global coverage, long-term
33 stability, and minimal bias (Kursinski et al., 1997; Anthes et al., 2008; Ho et al., 2020). By
34 measuring the bending of GNSS signals as they pass through the atmosphere, RO enables
35 retrievals of refractivity, temperature, pressure, and humidity profiles. As a limb-sounding
36 technique, it is largely unaffected by clouds and precipitation, providing an all-weather
37 observing capability essential for weather forecasting and climate monitoring (Cucurull et al.,
38 2007; Healy, 2008; Steiner et al., 2020).

39
40 Over the past two decades, the expansion of GNSS constellations (e.g., GPS, GLONASS,
41 Galileo, BeiDou) and the increasing availability of RO missions, including government-funded
42 programs (e.g., COSMIC-1/2, Metop-A/B/C, Sentinel-6) and commercial ventures (e.g., Spire,
43 GeoOptics, PlanetiQ), have significantly increased the volume of RO observations (Anthes,
44 2011; Schreiner et al., 2020; Ho et al., 2023). Today, global RO data counts exceed 35,000-
45 40,000 profiles per day, with substantial contributions from commercial providers through
46 initiatives such as NOAA's Commercial Data Purchase (CDP) program. While this growth
47 enhances the value of RO for numerical weather prediction (NWP) and climate applications, it
48 also introduces challenges due to differences in instrument design, tracking strategies,
49 sampling patterns, and processing methodologies.

51 RO retrievals involve several steps: i) deriving clock-synchronized excess phase and signal-to-
52 noise ratio (SNR) data, ii) inverting excess phase to bending angle (BA) profiles, and iii)
53 retrieving refractivity from BA via Abel or statistical methods (Gorbunov, 2002a). In the lower
54 troposphere, strong gradients and multipath propagation complicate retrievals, motivating
55 advanced inversion techniques such as Full Spectrum Inversion (FSI) (Jensen et al., 2003;
56 Adhikari et al., 2016, 2021), Canonical Transform Type 2 (CT2) (Gorbunov et al., 2005), and
57 Phase Matching (PM) (Jensen et al., 2004; Sokolovskiy et al., 2011). FSI relies on explicit
58 signal localization to enhance vertical resolution and mitigate multipath by reducing spectral
59 mixing, whereas CT2 achieves an implicit, physics-based localization in impact parameter
60 space, enabling more robust separation of multipath contributions. While FSI is designed to
61 leverage full-spectrum information for potentially enhanced sensitivity to fine-scale
62 atmospheric structures, it is also generally more noise-sensitive. CT2, in contrast, provides
63 more stable retrievals in strong multipath conditions, sometimes at the expense of reduced
64 small-scale resolution. Consequently, the effective vertical resolution of both methods is highly
65 dependent on specific implementation and tuning choices, such as filter settings and truncation
66 strategies. As a result, FSI is generally more sensitive to fine-scale atmospheric structures but
67 also more noise sensitive, while CT2 provides more stable retrievals in strong multipath
68 conditions at the expense of reduced small-scale resolution.

69
70 The international RO community is currently undertaking a coordinated effort to evaluate the
71 impact of large volumes of RO data on NWP. This initiative, known as the Radio Occultation
72 Modeling Experiment (ROMEX), is endorsed by the International Radio Occultation Working
73 Group (IROWG) (<https://irowg.org/ro-modeling-experiment-romex/>) and provides a
74 collaborative platform for data providers and processing centers to assess RO retrievals under
75 a standardized framework (Anthes et al., 2024). GNSS RO observations from a broad range of
76 government-funded and commercial missions were submitted to EUMETSAT for centralized
77 processing, and the resulting products were distributed via the Radio Occultation Meteorology
78 Satellite Application Facility (ROM SAF). ROMEX provides a standardized framework for
79 assessing inter-mission and inter-algorithm differences. Central questions include whether
80 assimilating larger RO volumes improves forecasts, and how variations in data quality and
81 inversion methods affect the outcome.

82
83 In support of ROMEX, the NOAA Center for Satellite Applications and Research (STAR)
84 contributed independent datasets processed using the FSI algorithm (RFSI), which was
85 integrated into version 10.0 of the Radio Occultation Processing Package (ROPP) (ROPP,
86 2020). This customized system, hereafter referred to as STAR ROPP, retains compliance with
87 ROPP standards while incorporating STAR-developed retrieval capability, including both the
88 CT2 and FSI methods for bending angle retrieval. Here, STAR RFSI denotes the STAR
89 implementation of the FSI-based bending angle retrieval, while STAR ROPP refers to the
90 customized ROPP v10.0 framework developed at STAR that supports both CT2 and FSI
91 processing. This system is distinct from the official ROM SAF ROPP, which serves as the
92 community standard. In this study, the community-standard dataset refers specifically to data
93 generated using the STAR ROPP CT2 method. Maintaining this distinction is essential, as it
94 enables an independent assessment of algorithmic effects on RO data quality.

95
96 FSI ~~offers is theoretically a specific approach well suited~~ for resolving fine-scale atmospheric
97 structures and handling multipath in the lower troposphere (Jensen et al., 2003; Adhikari et al.,
98 2021), a key source of uncertainty for NWP. The use of the STAR RFSI algorithm within
99 ROMEX is therefore to quantify the structural uncertainty associated with this alternative,
100 high-resolution retrieval approach, which is sensitive to small-scale features, relative to

101 community-standard methods, thereby providing critical insight for optimizing multi-mission
102 data assimilation strategies.

103

104 This study evaluates the STAR FSI-based processing system within the ROMEX framework.
105 Retrievals from RFSI are compared against those from the STAR ROPP with the CT2 method
106 and the EUMETSAT-processed ROMEX dataset (with COSMIC-2 data provided by UCAR).
107 The analysis focuses on November 2022 and utilizes the European Centre for Medium-Range
108 Weather Forecasts (ECMWF) Reanalysis v5 (ERA5) (Hersbach et al., 2023) as a reference to
109 evaluate algorithmic performance across various missions. The STAR RFSI dataset for
110 ROMEX is one of the three RO datasets, along with those from EUMETSAT and UCAR, that
111 were released to ROMEX participants through ROM-SAF (Shao and Folsche, 2024).

112

113 Intercomparisons included statistical evaluations (mean biases, standard deviations) and inter-
114 algorithm consistency. This design helps isolate processing-related uncertainties (e.g.,
115 structural uncertainty; Ho et al., 2012) and ensures that differences in NWP impact can be
116 attributed to data quality and processing methodology rather than uncontrolled input or
117 evaluation effects.

118

119 The paper is organized as follows: Session 2 describes the GNSS RO observations and datasets
120 used in this study. Session 3 presents the FSI algorithm in detail. Session 4 provides inter-
121 algorithm and inter-mission comparison results using ROMEX RO data. Conclusions are
122 summarized in session 5.

123

124 **2. GNSS RO Observations and Data Used in this Study**

125 **2.1 GNSS RO Observations**

126

127 Modern satellite missions, including COSMIC-2, Spire, and PlanetiQ, have significantly
128 increased the volume of GNSS radio occultation data. These missions track signals from
129 multiple constellations, including GPS, GLONASS, Galileo, and BeiDou, thereby improving
130 global spatial and temporal coverage for atmospheric profiling.

131

132 LEO satellite receivers track GNSS signals using two primary methods: Closed Loop (CL) and
133 Open Loop (OL). CL tracking ensures stable signal acquisition in the upper atmosphere but
134 may fail under rapidly varying conditions in the lower troposphere. OL tracking, by contrast,
135 is specifically designed to capture multipath-affected signals in the lower atmosphere. The
136 combination use of CL and OL tracking was traditionally adopted to ensure reliable
137 performance across the full vertical extent of the atmosphere. However, recent GNSS radio
138 occultation missions, including COSMIC-2, Spire, and PlanetiQ, primarily employ OL
139 tracking throughout the occultation in order to maximize tracking robustness and data
140 continuity across all atmospheric layers.

141

142 The raw data, consisting of signal phase and amplitude measurements, are processed to
143 calculate bending angle and refractivity profiles. A critical step in this process is correcting
144 ionospheric effects. This is achieved by using dual-frequency signals (e.g., L1 and L2), which
145 allow separation of the frequency-dependent ionospheric interference from the non-dispersive
146 signal of the neutral atmosphere. This isolation is essential for accurate atmospheric retrievals.

147

148 **2.2 RO Data Used in this Study**

149

150 This study utilizes Level 1b atmospheric excess phase data (in conPhs/atmPhs format) from
 151 the ROMEX campaign. The dataset includes contributions from commercial providers, such
 152 as PlanetiQ, Spire, and GeoOptics, as well as government-funded missions, including Metop-
 153 B/C and COSMIC-2. A summary of mission-specific data coverage for the period 1 September
 154 to 30 November 2022 is provided in Table 1. These excess phase datasets, delivered in NetCDF
 155 format and available exclusively to ROMEX participants, serve as the primary input for
 156 deriving neutral atmospheric bending angle and refractivity profiles. On average, the dataset
 157 comprises approximately 37,900 profiles per day.

158
 159 The high scientific value and cost-effectiveness of GNSS RO technology have driven increased
 160 private-sector participation in recent years. U.S. companies Spire Global, PlanetiQ, and
 161 GeoOptics, along with Yunyao Aerospace in China, have deployed RO receivers on
 162 commercial satellites to supply high-quality data to the scientific community. Among them,
 163 Spire Global Inc. contributes approximately 17,000 profiles per day to ROMEX, followed by
 164 Yunyao Aerospace with about 6,200, PlanetiQ with about 3,300, and GeoOptics with roughly
 165 300.

166
 167 Several government-funded RO satellite missions were routinely processed by the UCAR
 168 COSMIC Data Analysis and Archive Center (CDAAC) and made available to both the research
 169 and operational communities during the ROMEX period. These missions include COSMIC-2
 170 (~6,000 profiles/day), KOMPSAT-5 (~300), PAZ (~200), and both TerraSAR-X and
 171 TanDEM-X (~100 each). RO data from Metop-B/C and Sentinel-6 were provided by
 172 EUMETSAT, delivering approximately 1,200 and 800 profiles per day, respectively. RO
 173 profiles from FY-3C/D/E and Tianmu were supplied by the National Satellite Meteorological
 174 Center (NSMC) of the Chinese Meteorological Administration (CMA) and the National Space
 175 Science Center (NSSC) of the Chinese Academy of Sciences (CAS), respectively, with average
 176 daily counts of approximately 2,100 and 300.

177
 178 For this study, we processed RO data from all ROMEX missions except Sentinel-6 and
 179 GeoOptics, as well as from the Chinese government or Chinese companies (e.g., FY-3,
 180 Yunyao, and Tianmu). For each processed mission, we generated bending angle and
 181 refractivity profiles using both the STAR RFSI and STAR ROPP (CT2) algorithms. These
 182 datasets were submitted to EUMETSAT and distributed to ROMEX participants through the
 183 ROM SAF. By processing multiple missions with independent algorithms, we ensured
 184 consistent inputs across platforms. We enabled a direct assessment of algorithm-dependent
 185 uncertainties, thereby clarifying how data processing influences the interpretation of ROMEX
 186 NWP impact experiments. Table 2 summarizes the typical SNR characteristics of GNSS
 187 receivers across different missions, supporting the discussion of mission-dependent
 188 performance and structural uncertainties.

189
 190 Table 1: RO Missions are included in ROMEX

191

RO mission	RO profiles/day	Excess phase provider	STAR ROPP/RFSI	EUMETSAT
Metop B, C (GRAS)	1200	EUMETSAT	√	√
COSMIC-2	6000	UCAR	√	√ [#]
SPIRE	17000	Spire	√	√ [*]
PlanetiQ	3300	PlanetiQ	√	√ [*]
GeoOptics	300	GeoOptics	x	√

KOMPSAT-5	300	UCAR	√	√
PAZ	200	UCAR	√	√
TerraSAR-X	100	UCAR	√	√
TanDEM-X	100	UCAR	√	√
Sentinel-6	800	EUMETSAT	x	√
FY3-C, D, E (GNOS)	2100	CMA/NSMC	x	√
Yunyao	6200	Yunyao	x	√
Tianmu	300	CAS/NSSC	x	√
ROMEX total	37900			

192 √[#] UCAR provided both bending angle and refractivity in the EUMETSAT ROMEX dataset.

193 √* No refractivity available in the EUMETSAT dataset for PlanetiQ and Spire, only bending
194 angle

195

196 Table 2 Signal-to-Noise Ratio (SNR)[#] characteristics of GNSS receivers across different
197 missions

RO mission	GPS	GLONASS	Galileo	BeiDou
Metop B	730.2			
Metop C	789.3			
COSMIC-2	1295.1	1181.4		
SPIRE	387.9	707.2	316.4	
PlanetiQ	1440.5	1580.6	1124.8	1335.7
KOMPSAT-5	617.2			
PAZ	503.9			
TerraSAR-X	622.4			
TanDEM-X	549.3			

198 [#] Mean SNR between altitudes 60 km and 80 km, with unit (volt/volt)

199

200 3. Full Spectrum Inversion Algorithm and Processing Chain

201

202 The core FSI algorithm remains consistent with that described in Adhikari et al. (2021). The
203 novelty of the present work is not in the invention of the FSI algorithm, but in the
204 successful development and systematic application of the complete STAR RFSI end-to-end
205 processing framework and its subsequent inclusion in the ROMEX intercomparison as an
206 independent data source.

207

208 The scientific contribution is distinct from previous FSI work in three key ways. (1) Systematic
209 Multi-Mission Application: This study provides the first comprehensive, cross-mission
210 validation of the STAR RFSI system using a large and diverse ROMEX dataset (including
211 commercial and government-funded missions) against other major community processing
212 centers (such as EUMETSAT and UCAR). (2) Quantification of Structural Uncertainty: The
213 primary objective and scientific value of this study is the quantification of the structural
214 uncertainty among different processing approaches, FSI, STAR CT2, and the EUMETSAT
215 ROM SAF ROPP CT2, under a ROMEX framework. This analysis provides critical metrics
216 for interpreting ROMEX forecast impact studies. (3) Operational Documentation: The
217 manuscript documents the complete STAR RFSI processing chain (including data
218 preprocessing, quality control, and statistical optimization), which is essential for transparency
219 and future operational use within NOAA STAR. The novelty of the present work lies in the

development and presentation of the complete STAR RFSI end-to-end processing framework (including data preprocessing, quality control, and statistical optimization) and its systematic, harmonized application to the large and diverse multi-mission ROMEX dataset for comprehensive assessment of structural uncertainties against other major processing centers (such as EUMETSAT and UCAR). The STAR RFSI algorithm provides a robust framework for generating bending-angle and refractivity profiles from GNSS RO measurements, particularly in the presence of lower-tropospheric multipath. As described by Chen et al. (2024), the STAR RFSI algorithm has been integrated into ROPP version 10.0 customized at NOAA STAR. RFSI processes dual-frequency excess phase and SNR data along with satellite position and timing information. It supports a wide range of satellite missions and tracking configurations.

The STAR RFSI end-to-end process involves four main steps (see Fig. 1):

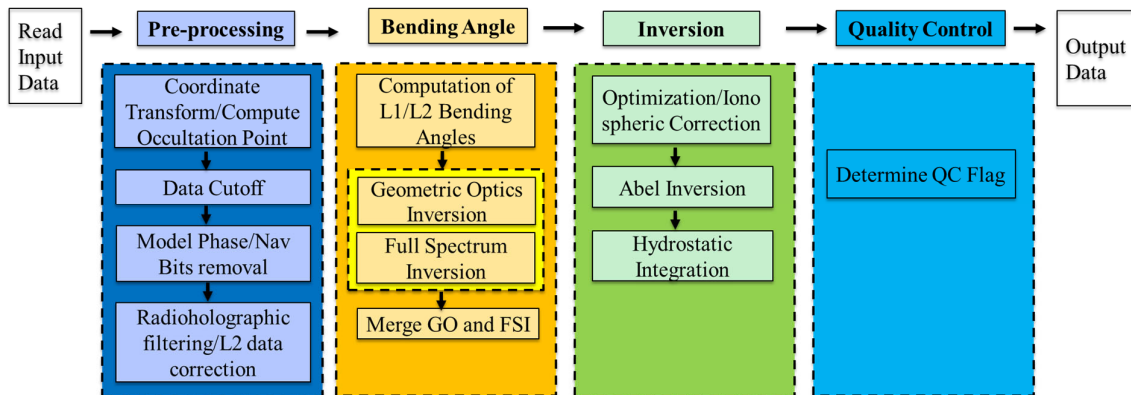
(1) data input and pre-processing: RO data, including satellite geometry, excess phase, and SNR measurements, are ingested and prepared for further processing. Satellite coordinates, if provided at lower frequencies, are interpolated to align with the sampling time using clock bias-corrected transmitter and receiver times (see Section 3.1).

(2) bending angle calculation: excess phase data are converted to bending angles, with ionospheric corrections applied using dual-frequency measurements (see Section 3.2).

(3) inversion to refractivity and dry temperature: bending angles are inverted using Abel integration to derive refractivity profiles, which can subsequently be used to compute dry atmospheric temperature (see Section 3.3).

(4) quality control (QC): a comprehensive quality assessment is conducted by applying quality flags based on threshold criteria for bending angle differences, determined through comparisons with ERA5 simulations. This process ensures that only high-quality profiles are retained as valid (see Section 3.4). Additionally, we have developed an internal quality control system designed explicitly for near-real-time processing. This internal check was not included in the ROMEX data when it was generated.

Figure 1 illustrates the complete RO data processing workflow implemented in the STAR FSI system, highlighting the transition from raw signal acquisition to the generation of quality-controlled atmospheric profiles (bending angle and refractivity).



257
258

259 Fig. 1: Flow chart depicting the steps used in the FSI RO data processing of the geometry and
 260 phase data.

261

262 3.1 Data Input and Pre-processing

263

264 The STAR RFSI system ingests Level 1b dual-frequency excess phase and SNR data, along
 265 with satellite position and time information, to generate high-resolution atmospheric profiles.
 266 The geometry files typically contain satellite position vectors at a lower sampling rate (e.g., 1
 267 Hz), whereas the excess phase and SNR are sampled at higher rates (e.g., 50-100 Hz). To align
 268 these data, satellite coordinates are interpolated to the excess-phase sampling times using
 269 clock-bias-corrected receiver and transmitter times. Satellite geometry and excess phase/SNR
 270 time series are interpolated into a common sampling rate. Given start time (t_s), sampling time
 271 (t), and clock bias-corrected receiver time (t_{orb}) and transmitter time (t_{txm}), the interpolated
 272 receiver coordinates (r_{leo}), transmitter time (t_{txmHR}), and GNSS coordinates (r_{gns}) can be
 273 calculated using cubic spline interpolation as:

274

$$275 \quad r_{leo} = \text{interpolate}(r_{leoLR}, t_{orb}, t + t_s, /cubic_spline) \quad (1)$$

276

$$277 \quad t_{txmHR} = \text{interpolate}(t_{txm}, t_{orb}, t + t_s) \quad (2)$$

278

$$279 \quad r_{gns} = \text{interpolate}(r_{gnsLR}, t_{txm}, t_{txmHR}, /cubic_spline) \quad (3)$$

280

281 where r_{leoLR} and r_{gnsLR} are the original coordinates.

282

283 The time series of satellite positions is initially provided in the Earth-Centered Inertial (ECI)
 284 J2000 frame. These positions are converted to Earth-Centered Earth-Fixed (ECEF) coordinates
 285 according to the IERS 2010 conventions, which include corrections for polar motion and Earth
 286 rotation (Adhikari et al., 2021; Petit and Luzum, 2010; Luzum and Petit, 2010). This
 287 transformation enables geolocation of the occultation tangent point at each time step.

288

289 To satisfy the assumption of local spherical symmetry during inversion, occultation geometry
 290 is reprojected to the local center of curvature. The tangent point location on the reference
 291 ellipsoid (WGS84) is determined where the straight line between the transmitter and receiver
 292 touches the ellipsoid. The latitude, longitude, local radius of curvature, and the center of
 293 curvature are computed at this reference tangent point and used to shift both GNSS and LEO
 294 positions into a local spherical coordinate system. This step ensures accurate mapping of
 295 impact parameters and tangent altitudes for each ray path.

296

297 RO signals acquired using OL tracking may contain low-SNR regions near the surface due to
 298 signal fading or tracking loss (see Figure 5 in Adhikari et al., 2021). An appropriate cut-off
 299 height is essential to ensure the accuracy and reliability of tropospheric information retrieved
 300 from GNSS signals in OL tracking mode (Sokolovskiy et al., 2009; Sokolovskiy et al., 2010;
 301 Adhikari et al., 2021; Paoletta et al., 2025). To prevent the propagation of noise-contaminated
 302 signals through the inversion chain, a systematic signal truncation method is employed using
 303 SNR-based thresholds in this study. The truncation procedure includes the following steps: (1)
 304 initial cut-off impact height: the initial threshold of impact height is set based on the LEO
 305 satellite's altitude, as it influences the signal's penetration depth and the quality of retrieved
 306 atmospheric profiles; (2) dynamic background SNR calculation: the background SNR is
 307 estimated for each time series using the lowest 10 seconds of the smoothed data. A 3-second
 308 moving average is applied to the time series to smooth out high-frequency fluctuations; (3)

309 initial SNR threshold determination: starting from the lowest point in the time series, the first
 310 point where the SNR exceeds three times the calculated background SNR in step (2) is
 311 identified as a preliminary threshold. (4) final cut-off point selection: moving backward from
 312 the uppermost point identified in step (3), the cut-off point is determined as the first point where
 313 the SNR drops below 1.5 times the background SNR, and the associated impact height is higher
 314 than the threshold established in step (1).

315

316 This filtering removes anomalous low-level SNR spikes, which can occur due to OL tracking
 317 artifacts, particularly in tropical and high-humidity conditions. Improper truncation can
 318 degrade the quality of bending angle measurements: truncating too high removes real signals,
 319 introducing a negative bias, while truncating too low retains noise, leading to oscillations in
 320 the retrieved profiles. The chosen thresholds aim to maximize vertical coverage without
 321 sacrificing data quality.

322

323 **3.2 Computation of Bending Angles using Full Spectrum Inversion**

324

325 Bending angle retrieval is performed in two steps: (1) computation of the model phase and
 326 correction of navigation bit jumps, and (2) inversion of observed signals using FSI to retrieve
 327 bending angles as a function of impact parameter.

328

329 **3.2.1 Calculation of model phase**

330

331 The model phase is derived from a reference refractivity profile computed using the MSIS-90
 332 climatology (Hedin, 1991), assuming 90% relative humidity below 15 km. Refractivity (N) is
 333 calculated as

334

$$335 \quad N = 77.6 \frac{P}{T} + 3.73 \times 10^5 \frac{e}{T^2} \quad (4)$$

336

337 where P is pressure, T is temperature, and e is water vapor. The model impact parameter (a) at
 338 altitude z is calculated as

339

$$340 \quad a = n(R + z) = nr, \quad (5)$$

341

342 where, $n = 1 + N \times 10^{-6}$, R is the local radius of curvature of the Earth, and $r = R + z$.

343

344 The bending angle (α) profile is derived from n and a using Abel integration

345

$$346 \quad \alpha(p) = 2p \int_{r_1}^{\infty} \frac{a}{\sqrt{n^2 r^2 - a^2}} \frac{dn(n)}{dr} dr, \quad (6)$$

347

348 The impact parameter and bending angle profiles, along with occultation time (t), satellite
 349 positions, and velocities, are then used to derive the Doppler shift associated with the
 350 atmospheric refractivity $n(z)$. The model phase, computed from occultation time and the
 351 Doppler shift, provides a reference for identifying navigation bit jumps.

352

353 In most RO data, navigation bits embedded in the excess phase and coordinate time series can
 354 introduce discontinuities of $\pm\pi$. These phase jumps are identified by comparing the measured
 355 excess phase with the model phase, especially at high sampling rates (≥ 50 Hz). Once detected,
 356 the navigation bit pattern is applied to correct discontinuities in the measured phase, ensuring
 357 continuity and accuracy in the processed phase time series. Although the MSIS model is used
 358 to calculate the reference phase for these corrections, it introduces a known source of
 359 uncertainty in the lower troposphere. This uncertainty highlights the critical need for an
 360 external navigation bit stream, since standard navigation-bit-free cycle slip correction routines
 361 (such as those in ROPP) often struggle with atmospheric multipath in this region. To mitigate
 362 this issue, processing is often terminated above a 7-10 km impact height. However, this
 363 challenge can be circumvented by using pilot signals (Galileo E1C and E5BQ, GPS L2C, and
 364 BeiDou B1CP and B2AP), which are not modulated with navigation bits and can therefore
 365 yield reliable results in the lower troposphere even without external bit stream data (Jonathan
 366 Brandmeyer, personal communication, June 2025).

368 369 **3.2.2 Full Spectrum Inversion**

370
 371 To retrieve bending angles from RO signals, it is essential to reduce high-frequency noise in
 372 the excess phase. This is typically achieved using low-pass or radio-holographic filters
 373 (Gorbunov et al., 2005). In the current RFSI inversion system, a 0.5-second low-pass Fourier
 374 filter is applied to the excess Doppler signal (the time derivative of excess phase). The filtered
 375 Doppler is then reintegrated to recover a smoothed excess phase. The 0.5-second window
 376 approximately matches the vertical resolution of RO observations, corresponding to the first
 377 Fresnel zone (Kursinski et al., 1997). To better resolve fine-scale refractivity structures in the
 378 lower atmosphere, a shorter, height-dependent smoothing window is used below 10 km: 0.05
 379 seconds for 100 Hz data and 0.1 seconds for 50 Hz, enabling noise reduction while preserving
 380 small-scale features. The choice of these parameters is based on systematic tuning experiments
 381 in which multiple configurations were evaluated. The selected values showed here provide the
 382 most consistent statistical agreement with model outputs, such as ERA5, yielding reduced
 383 bending angle bias and standard deviation compared with other tested configurations.

384
 385 Bending angles are computed using geometric optics (GO) above 25 km and the full spectrum
 386 inversion method below this altitude. In FSI, the received signal is expressed as a sum of
 387 narrowband sub-signals in the open-angle domain θ :

$$388 \quad u(\theta) = \sum_p A_p(\theta) e^{i\varphi_p(\theta)} \quad (7)$$

389
 390 where, A_p and φ_p are the amplitude and phase of the p th sub-signal, respectively. The Fourier
 391 transform of Eq. (7) is:

$$392 \quad F(\hat{\omega}) = \sum_p \int_{\theta_1}^{\theta_2} A_p(\theta') e^{i(\varphi_p - \hat{\omega}')} d\theta' \quad (8)$$

393
 394 where θ_1 and θ_2 represent the open angles at the start and end of the occultation, respectively.

395
 396 Applying the method of stationary phase (MSP) (Born and Wolf, 1999; Jensen et al., 2003),
 397 the transform simplifies to:

398
 399
 400

401
$$F(\hat{\omega}) \approx B e^{i(\varphi_q - \hat{\omega}_q \theta_s)} \quad (9)$$

402

403 where B is an approximately constant amplitude, and the pseudo frequency $\hat{\omega}_q$ satisfies

404

405
$$\hat{\omega}_q = \left. \frac{d\varphi_q}{d\theta} \right|_{\theta=\theta_s} \quad (10)$$

406

407 The stationary points θ_s is then given by:

408

409
$$\theta_s = -\frac{d\psi}{d\hat{\omega}}, \text{ where } \psi = \varphi_q - \hat{\omega}_q \theta_s \quad (11)$$

410

411 The derivative of the phase (φ_q) with respect to θ , accounting for the signal path from the
412 GNSS to LEO satellite, is:

413

414
$$\frac{d\varphi_q}{d\theta} = \hat{\omega}_q = ka + k \frac{dR_L}{d\theta} \sqrt{1 - \left(\frac{a}{R_L}\right)^2} + k \frac{dR_G}{d\theta} \sqrt{1 - \left(\frac{a}{R_G}\right)^2}, \quad (12)$$

415

416 where k is the wavenumber of the carrier signal, R_L and R_G are the distances from the GNSS
417 and LEO satellites to the local center of curvature, respectively, and a is the impact parameter.

418

419 Assuming circular orbits, the derivatives of R_L and R_G vanish, reducing Eq. (12) to:

420

421
$$\frac{d\varphi_q}{d\theta} = ka \quad (13)$$

422

423 Differentiating with respect to $\hat{\omega}$ gives:

424

425
$$da = \frac{1}{k} d\hat{\omega}, \quad (14)$$

426

427 The spectral resolution of the Fourier transform phase, $d\hat{\omega}$, is given by (Adhikari et al. 2016):

428

429
$$d\hat{\omega} = \frac{2\pi}{\Delta\theta}, \text{ where } \Delta\theta = \theta_2 - \theta_1 \quad (15)$$

430

431 Finally, with the impact parameter a and the open angle θ , the bending angle is computed as:

432

433
$$\alpha(a) = \theta + \arcsin\left(\frac{a}{R_L}\right) + \arcsin\left(\frac{a}{R_G}\right) - \pi. \quad (16)$$

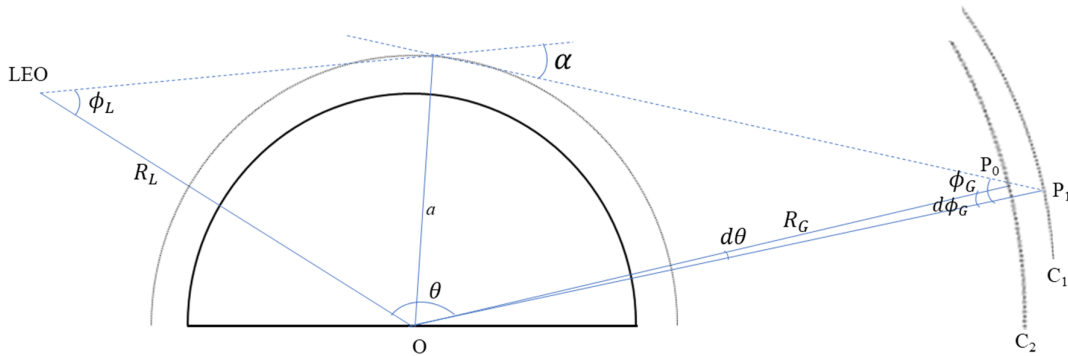
434

435 **3.2.3 Correction for non-spherical trajectory**

436

437 The assumption underlying Eq. (16) is invalid in realistic occultation scenarios due to the
438 Earth's oblateness and the non-coplanar nature of GNSS and LEO satellite orbits. To account
439 for these effects, a correction must be applied to the observed phase to project the signal path
440 onto circular, coplanar trajectories. As illustrated in Fig. 2, the actual GNSS satellite orbit is
441 represented by arc C_1 , with each point along the trajectory projected onto a circular orbit, C_2 .
442 Notably, the impact parameter (a) remains unchanged during this projection. In this process,
443 the GNSS position is shifted from P_1 on arc C_1 to P_0 on arc C_2 . This projection alters the open
444 angle (θ), the signal ray (ϕ_G), and the phase of the signal. Although Fig. 2 focuses on the GNSS
445 orbit, the same projection method is also applied to the LEO receiver orbit. Given the known

446 positions of the GNSS and LEO satellites, the resulting changes in phase and open angles can
 447 be determined geometrically. Note that the radius and center of curvature are treated as fixed
 448 for a given RO event and are not dynamically reprojected. The projection is performed with
 449 respect to the precomputed local center of curvature, ensuring a consistent coordinate system
 450 throughout the inversion process.



451
 452 Fig. 2: Projection of a non-circular orbit relative to the local center of curvature to a circular
 453 orbit.

454
 455 After calculating bending angles for the L1 and L2 frequencies separately, the profiles are
 456 truncated using the FSI amplitude. This step is necessary because the FSI method produces
 457 bending angle and impact parameter pairs over an infinite range of impact parameters.
 458 Determining the lowest impact parameter and its corresponding bending angle is critical. In the
 459 current STAR FSI inversion approach, the pair with the lowest impact parameter and bending
 460 angle is identified based on the amplitude of the Fourier transform. The amplitude is first
 461 normalized using the signal's mean amplitude within the 10-50 km range. The lowest point is
 462 defined as the altitude at which the normalized amplitude drops below 0.35. This threshold is
 463 empirically determined based on extensive testing within the STAR FSI system. It represents
 464 an optimal balance between maximizing vertical penetration depth and minimizing noise-
 465 induced artifacts into the retrieved bending angle profile.

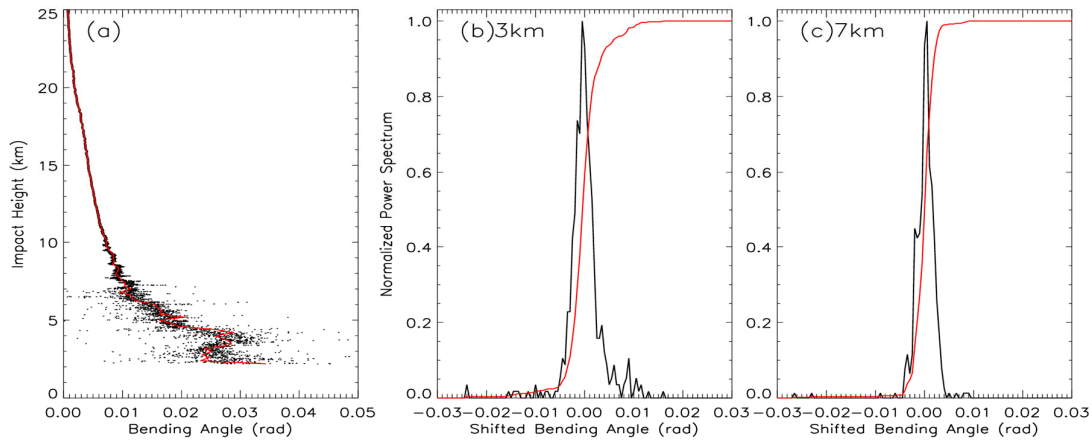
466 3.2.4 Bending Angle Uncertainty Calculation

467
 468 The uncertainty in the bending angle is estimated using a sliding spectrogram with a 500 m
 469 window. First, a smoothed bending angle profile is generated to identify the central component.
 470 Then, the bending angle from the unsmoothed signal is calculated at 1 m impact height
 471 resolution. With each spectral window, deviations from the central component are used to
 472 construct a local power spectrum of the shifted bending angle, computed using a finite bending
 473 angle increment ($\delta\alpha = 0.0005$ rad). The shifted bending angle (α_s), is defined as the
 474 instantaneous bending angle minus the central component. The spectral width (Δs) is
 475 determined as the mean of the absolute value of the shifted bending angle weighted by the
 476 spectral power (ρ) of each component, as follows (which is similar to Liu et al. (2018)):
 477

$$478 \Delta s = \sqrt{\frac{\sum_{i=1}^n \rho_i \alpha_s^2 \delta\alpha}{\sum_{i=1}^n \rho_i \delta\alpha}} \quad (17)$$

480
 481 Figure 3(a) presents a representative bending angle profile at 1 m resolution as a function of
 482 the impact height (black dots), along with its central component (red line). Figure 3(b) and 3(c)
 483 show the corresponding normalized power spectrum (black line) and accumulated power
 484 spectrum (red line) at impact heights of 3 km and 7 km, respectively. As illustrated, the spectral

485 range at 3 km is broader than at 7 km, indicating greater atmospheric variability at lower
 486 altitudes. The bending angle uncertainty is quantified as half the spectral width, calculated
 487 using Eq. (17).
 488



489
 490 Fig. 3: (a) Spectrogram of the RO signal, power spectrum at (b) 3 km, and (c) 7.5 km impact
 491 heights.

492 3.3 Bending angle Inversion

493 3.3.1 Ionospheric Correction and Optimization

494
 495 To remove first-order ionospheric effects, and as an approximation for the neutral atmosphere
 496 bending angle, a linear combination of L1 and L2 bending angles ($\alpha_1(a)$ and $\alpha_2(a)$) is
 497 computed (Vorob'ev and Krasil'nikova, 1994):
 498
 499

$$500 \alpha_{LC}(a) = \frac{\alpha_1(a)f_1^2 - \alpha_2(a)f_2^2}{f_1^2 - f_2^2} \quad (18)$$

501 where f_1 and f_2 are the RO frequencies.

502 This is followed by statistical optimization (Gorbunov, 2002c):

$$503 \alpha(a) = \alpha_{BG}(a) + \frac{\sigma^S}{\sigma^S + \sigma^N} (\alpha_{LC}(a) - \alpha_{BG}(a)) \quad (19)$$

504
 505 where, σ^S and σ^N are the covariances of the neutral atmospheric signal and residual noise,
 506 respectively, and $\alpha_{BG}(a)$ is the background bending angle from a climatological model (MSIS-
 507 90 model).
 508

509 Covariance matrices are estimated from the deviation ($\Delta\alpha$) of L1 and L2 bending angles from
 510 the background model ($\alpha_{L1,L2} - \alpha_m$). For ionospheric signal and noise, deviations in the impact
 511 heights (impact parameter minus local center of curvature) of 50-70 km are used; for neutral
 512 atmospheric signal, the 12-35 km range is used. In the lower troposphere, near the surface,
 513 where the L2 signals weaken, a constant correction is applied based on the lowest valid L2
 514 altitude.
 515
 516
 517
 518
 519

520 **3.3.2 Abel Inversion**

521

522 Refractivity is retrieved from ionosphere-corrected bending angles using the Abel transform
 523 (Fjeldbo et al., 1971). The bending angle profile is extended up to 150 km using climatological
 524 data (MSIS-90 model) to stabilize the upper boundary condition. Tangent point locations are
 525 recovered by interpolating the occultation time and satellite positions. Since time information
 526 is lost during the Fourier transform of the RO signal, the occultation time is reconstructed from
 527 the bending angle-impact parameter profile and used to infer the latitude and longitude of each
 528 tangent point.

529

530 **3.4 Quality control**

531

532 Due to the lack of effective internal quality control in the ROPP v10 package, we rely on
 533 external quality control procedures to identify bad profiles. The fractional difference between
 534 the observed (O) and simulated (B) bending angles, calculated from ERA5 forecast fields, is
 535 used to assess the quality of the RO data at each altitude level:
 536

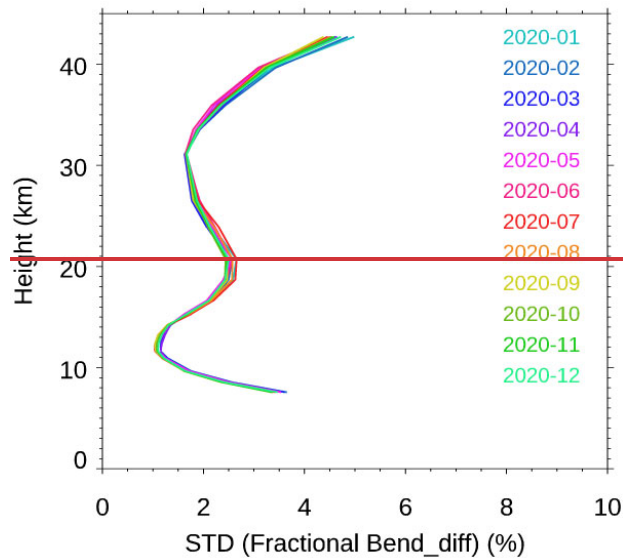
537

$$BA_{diff} = \frac{O-B}{B} \quad (20)$$

538

539 ~~Figure 4 shows the monthly mean standard deviation of the fractional bending angle~~
 540 ~~differences for 2020, from 8 to 43 km altitude.~~ The annual mean standard deviation (σ_{year}) from
 541 2020 is used as a benchmark. A profile is flagged as ‘bad’ if the bending angle difference
 542 exceeds $7\sigma_{year}$ at any altitude level between 10 and 40 km, where RO data quality is highest
 543 and model-observation agreement is strongest. A sensitivity study confirmed that using a 7σ
 544 year threshold provides an optimal balance between data retention and data quality.

545



546

547 ~~Fig. 4. Monthly standard deviation of the fractional bending angle differences in 2020.~~

548

549 In addition, profiles are also flagged as ‘bad’ under any of the following conditions: (1) The
 550 fractional BA difference exceeds $7\sigma_{year}$; (2) The top height of the profile is below 20 km; (3)
 551 The bottom height is above 20 km; and (4) A negative bending angle is detected below 50 km.
 552 The QC rejection rate for the ROMEX dataset depends on the mission. For example, the QC

553 pass rates are 85.7%, 94.8%, and 93.9% for COSMIC-2, Spire, and PlanetiQ, respectively.
 554 These values are comparable to those from CDAAC-processed data: 87.6%, 95.7%, and 90.6%,
 555 respectively. Note that quality control is not applied to PlanetiQ and Spire data processed by
 556 EUMETSAT. To ensure a consistent comparison in this study (Section 4), we applied our
 557 standard quality control procedure to the EUMETSAT dataset where quality control was
 558 absent.

559
 560
 561

562 It is important to note that this quality control procedure applies only to bending angles within
 563 a specific height range (10-40 km). In rare cases, even when the bending angle passes QC,
 564 anomalies in refractivity or dry temperature may still occur due to limitations in the Abel
 565 inversion. Future updates to the QC procedures will address such issues. This process ensures
 566 that only high-quality profiles are retained as valid. An internal quality control system tailored
 567 for near-real-time processing is under development; however, it was not incorporated into the
 568 ROMEX data when that dataset was produced.

569

570 4. Comparison Results

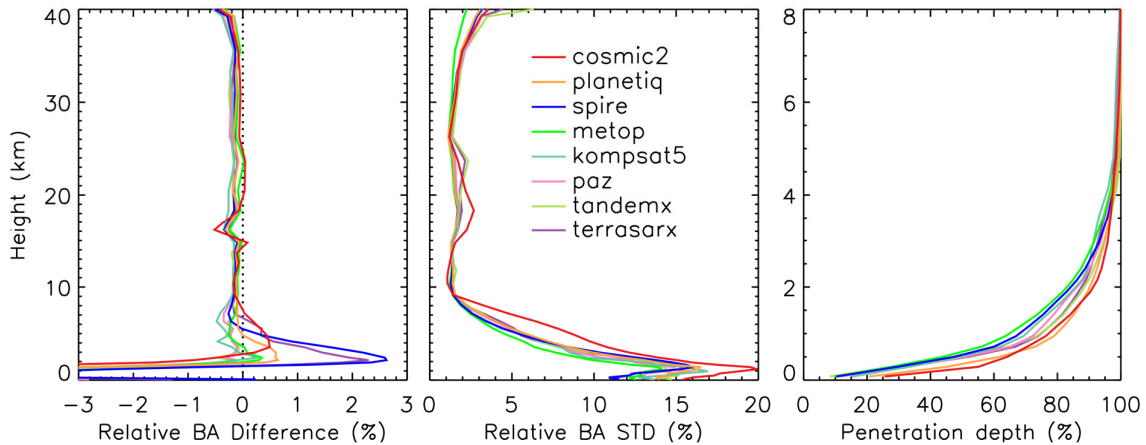
571

572 4.1 Bending angle comparison with STAR RFSI, STAR ROPP, and EUMETSAT

573

574 Figure 54 shows the height-dependent fractional bending angle differences between RO
 575 observations and ERA5 background fields (O-B) for multiple satellite missions processed
 576 using the RFSI algorithm during November 2022. The selected missions include COSMIC-2,
 577 Spire, PlanetiQ, Metop-B, Metop-C, Kompsat5, PAZ, TerraSAR-X, and TanDEM-X. The
 578 comparison serves as a proxy for evaluating the quality and inter-mission consistency of RFSI-
 579 processed RO data relative to a widely used global reanalysis.

580



581

582 Fig. 54. Comparison of height-dependent fractional bending angle between RO observations
 583 and ERA5 simulations (O-B) among different RO missions. BA mean biases (left), standard
 584 deviations (middle) in terms of fractional BA difference (%), and (right) penetration depth
 585 below 8 km for RFSI over November 2022.

586

587 In the middle and upper troposphere through the lower stratosphere (8-35 km), all missions
 588 exhibit excellent agreement with ERA5. Mean O-B differences are generally within $\pm 0.2\%$,
 589 and standard deviations remain below 3%, indicating high internal consistency among the RO
 590 datasets and strong alignment with ERA5 in this well-observed atmospheric region.

591

592 In the lower troposphere (below 8 km), larger biases and variability are evident, especially near
593 the surface. Spire and TerraSAR-X show mean biases up to 1-2% at 2 km, with standard
594 deviations exceeding 10%. COMSIC-2 exhibits the highest variability in this region, with
595 standard deviations approaching 20% at approximately 1 km. These discrepancies are likely
596 attributed to increased atmospheric variability in the lower troposphere, limitations in signal
597 tracking during multipath propagation at tropical/subtropical regions where high water vapor
598 variability makes OL tracking difficult, and the sensitivity of bending angle retrievals to SNR
599 cut-off thresholds. In contrast, PlanetiQ, Metop-B, and Metop-C demonstrate smaller near-
600 surface biases (typically <0.5%) and reduced variability, suggesting robust signal tracking
601 and/or more effective pre-processing of low-altitude data.

602

603 Above 35 km, mean biases increase to approximately 0.6%, and standard deviations increase
604 with height and can exceed 5% at 40 km. These deviations are primarily due to limitations in
605 ionospheric correction at higher altitudes, where residual ionospheric effects are more
606 challenging to remove completely. The ionospheric conditions during September-November
607 2022 were generally moderate and typical for the ascending phase of Solar Cycle 25, but
608 intermittently disturbed (including several geomagnetic storms and enhanced irregularities).
609 They are not representative of worst-case conditions, but also not purely quiet-average; they
610 are better described as moderately active with episodic disturbances.

611

612 Among the evaluated missions, PlanetiQ consistently shows low mean biases and standard
613 deviations across nearly the entire vertical range, indicating strong data stability and processing
614 robustness. Metop-B and Metop-C also exhibit excellent performance, likely due to mature
615 sensor platforms and the use of well-established pre-processing procedures in the ROPP
616 system. Spire data, while reliable in the mid- to upper troposphere, shows elevated near-surface
617 variability, likely due to its higher sensitivity to excess phase pre-processing (e.g., cycle-slip
618 removal and parameter tuning).

619

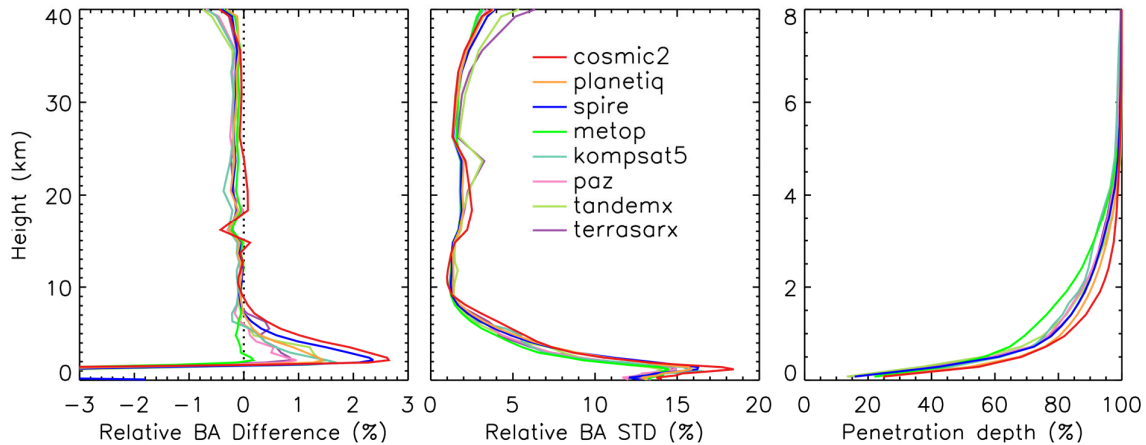
620 COSMIC-2 displays distinct behavior relative to other missions, with positive biases of 8-35
621 km and increased variability near the tropopause. These features are likely influenced by its
622 low-inclination orbit and limited latitudinal coverage ($\pm 45^\circ$), which concentrates observations
623 in tropical and subtropical regions with higher atmospheric variability. Similar features and
624 their impact on data assimilation performance have been discussed in previous studies (Ho et
625 al., 2023; Miller et al., 2025).

626

627 The penetration depth is defined as the minimum height above ground level where a valid (i.e.,
628 not filled or missing) bending angle or refractivity is obtained for a given RO event. Smaller
629 penetration depths indicate that the RO signal reaches closer to the Earth's surface. Penetration
630 depth depends on the signal cutoff criteria applied during processing (see Sections 3.1 and
631 3.2.3); therefore, comparisons among different missions should be made using the same
632 processing center and algorithm. The right panel of Figure 54 shows the penetration depth
633 profile below 8 km, expressed as the percentage of profiles reaching different altitudes relative
634 to 8 km, for the FSI method. As discussed by Gorbunov et al. (2022a, 2022b), higher SNR
635 generally improves tropospheric penetration. Consistent with Table 2, COSMIC-2 and
636 PlanetiQ exhibit the greatest penetration depth among the missions. Most missions achieve
637 more than 80% of occultations reaching 2 km or lower, and more than 50% reaching 1 km or
638 lower. The penetration depths are noticeably higher for Metop-B and Metop-C (green line),
639 while Spire, despite having the lowest SNR, achieves a slight better penetration than Metop.

640

641 Figure 65 shows O-B bending angle differences for the same missions and period, but with
 642 data processed using the STAR ROPP-CT2 method. The vertical structure of mean biases and
 643 variability is broadly similar to that in the RFSI results, reflecting consistent retrieval behavior
 644 between the two approaches. In the 8-35 km range, both methods yield small biases (within
 645 $\pm 0.2\%$) and standard deviations below 3%, confirming the reliability of both retrievals in the
 646 core atmospheric region. One exception is KOMPSAT-5, which shows a slight negative bias
 647 ($\sim -0.2\%$) between 17 and 23 km.
 648



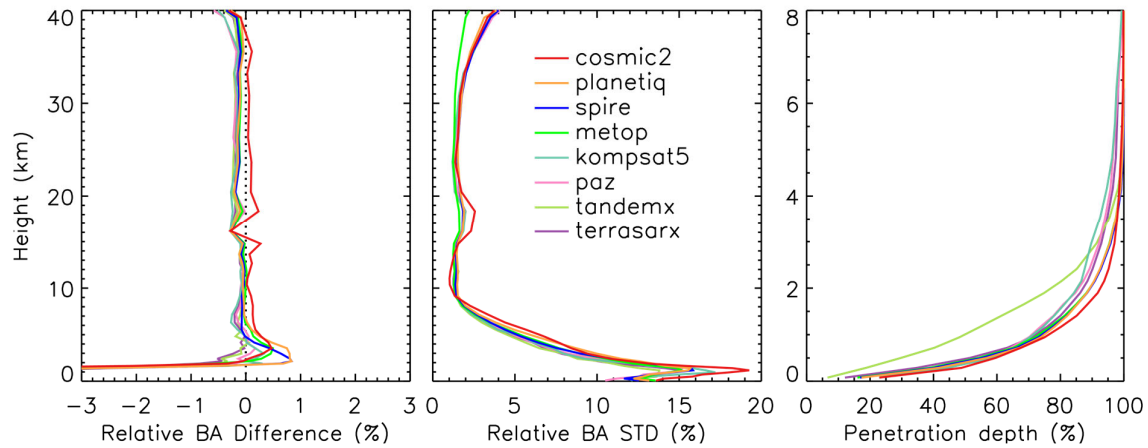
649
 650 Fig. 65. Same as Fig. 54, but for RO data generated from the ROPP package using the CT2
 651 method.

652
 653 Standard deviations increase above 35 km and below 8 km in both datasets, highlighting
 654 common challenges in the upper and lower atmospheric regions, including multipath effects,
 655 signal noise, and uncertainty in ionospheric corrections. However, the CT2 retrievals generally
 656 exhibit larger near-surface biases than those of RFSI. For all missions except Metop-B and
 657 Metop-C, the CT2-processed profiles exhibit biases of 1-2% near the surface, likely due to the
 658 more conservative use of signals and stronger smoothing.

659
 660 In contrast to Fig. 54, the penetration depth profiles among missions are much narrower below
 661 1 km, indicating that CT2 is less sensitive to SNR. Consistent with Fig. 54, COSMIC-2 and
 662 PlanetiQ show the deepest penetration depth among the missions. The penetration depths are
 663 noticeably higher for Metop-B and Metop-C than for Spire.

664
 665 Figure 76 displays ERA5 O-B differences for RO profiles processed by EUMETSAT, covering
 666 the same missions and period. The EUMETSAT-processed data (excluding COSMIC-2)
 667 utilized ROM SAF ROPP as the internal processing system, employing the CT2 method in the
 668 troposphere. Like Consistent with the other two datasets, EUMETSAT results show high
 669 consistency in the 8-35 km range, with mean biases within $\pm 0.2\%$ and standard deviations
 670 below 3%. COSMIC-2 again stands out, showing a positive bias of $\sim 0.2\%$, while most other
 671 missions exhibit slightly negative biases, suggesting a systematic offset in COSMIC-2 data
 672 relative to the ensemble.

673



674 Fig. 76. Same as Fig. 54, but for RO data provided from EUMETSAT.
 675
 676

677 In the lower troposphere, EUMETSAT retrievals exhibit the smallest mean biases (<1% at 2
 678 km) among the three datasets, suggesting more effective mitigation of noise and multipath
 679 effects near the surface. By comparison, RFSI-processed profiles for Spire and TerraSAR-X
 680 show near-surface biases of up to ~2%, while STAR ROPP CT2 retrievals yield 1-2% biases
 681 for most missions. COSMIC-2 exhibits high variability below 8 km across all three datasets,
 682 although the CT2 method appears to reduce it slightly. Note that while STAR ROPP and
 683 EUMETSAT ROPP both use CT2 method in the troposphere, their specific configuration
 684 parameters may differ.
 685

686 Above 35 km, the bending angle uncertainty increases in all datasets. However, EUMETSAT
 687 results exhibit more uniform performance across missions, with mean biases generally below
 688 0.5% and smaller inter-mission variability. Metop-B and Metop-C show the lowest standard
 689 deviations across all datasets in this altitude range, indicating highly stable performance at high
 690 altitudes.
 691

692 The penetration depth from TanDEM-X is noticeably higher than that of other missions in the
 693 EUMETSAT-processed data. For Metop-B and Metop-C, penetration depths are substantially
 694 improved compared with STAR FSI and STAR ROPP CT2, and approach those of COSMIC-
 695 2 and PlanetiQ below 1.5 km.
 696

697 The comparatively shallower penetration depths observed for Metop (in Fig. 5) and TanDEM-
 698 X (in Fig. 6) relative to missions like COSMIC-2 and PlanetiQ are linked to a combination of
 699 mission-specific characteristics (specifically SNR) and the data truncation strategies employed
 700 by the processing algorithm: 1) Impact of lower SNR: Penetration depth is fundamentally
 701 dependent on the signal cutoff criteria applied during processing, and higher SNR is known to
 702 improve tropospheric penetration. Metop-B/C and TanDEM-X exhibit lower mean SNRs (e.g.,
 703 Metop-B GPS SNR is 730.2, TanDEM-X is 549.3) compared to the missions with the deepest
 704 penetration (COSMIC-2 at 1295.1 and PlanetiQ at 1440.5). This lower SNR makes them more
 705 susceptible to noise and multipath effects in the lower troposphere, leading to a shallower
 706 signal cutoff. 2) Truncation strategy: The systematic signal truncation used in the STAR RFSI
 707 method is based on SNR thresholds to prevent noise-contaminated signals from propagating.
 708 For lower-SNR missions like Metop and TanDEM-X, these thresholds are reached at higher
 709 altitudes, resulting in shallower penetration. 3) Processing algorithm variation: The choice of
 710 processing algorithm also contributes to variation. The CT2 method, used in both ROPP
 711 systems (STAR ROPP and ROM SAF ROPP), is less sensitive to SNR and resulted in generally

narrower penetration depth profiles below 1 km compared to RFSI. This is further reflected by the fact that Metop-B/C penetration is substantially improved when processed by EUMETSAT's CT2 compared to STAR's algorithms, suggesting differences in the specific configuration parameters used by the processing centers.

-Together, these intercomparisons highlight key trade-offs among the different retrieval approaches. The RFSI method leverages the full frequency content of the RO signal, offering enhanced sensitivity to fine-scale atmospheric features. However, it is also more sensitive to noise, particularly near the surface. In contrast, the STAR ROPP CT2 method employs a canonical transformation that simplifies retrieval but is more conservative in its use of signal data, resulting in smoother profiles and slightly larger near-surface biases. EUMETSAT's processing strikes a balance between these extremes, achieving consistent results across the full vertical range while effectively suppressing noise in the lower troposphere and upper stratosphere.

4.2 Refractivity comparison with STAR RFSI, STAR ROPP, and EUMETSAT

Figure 87 presents the fractional refractivity differences between RO observations processed using the RFSI algorithm and ERA5 background fields for November 2022. The vertical structures of refractivity O-B statistics largely mirror those of the bending angle differences shown in Fig. 54, reflecting the propagation of bending angle quality into the refractivity retrieval. In the well-constrained 8-30 km region, all missions show excellent agreement with ERA5. Mean biases remain within $\pm 0.15\%$, and standard deviations are typically below 1%, indicating that refractivity retrievals in this core region retain the stability and consistency of the underlying bending angle data.

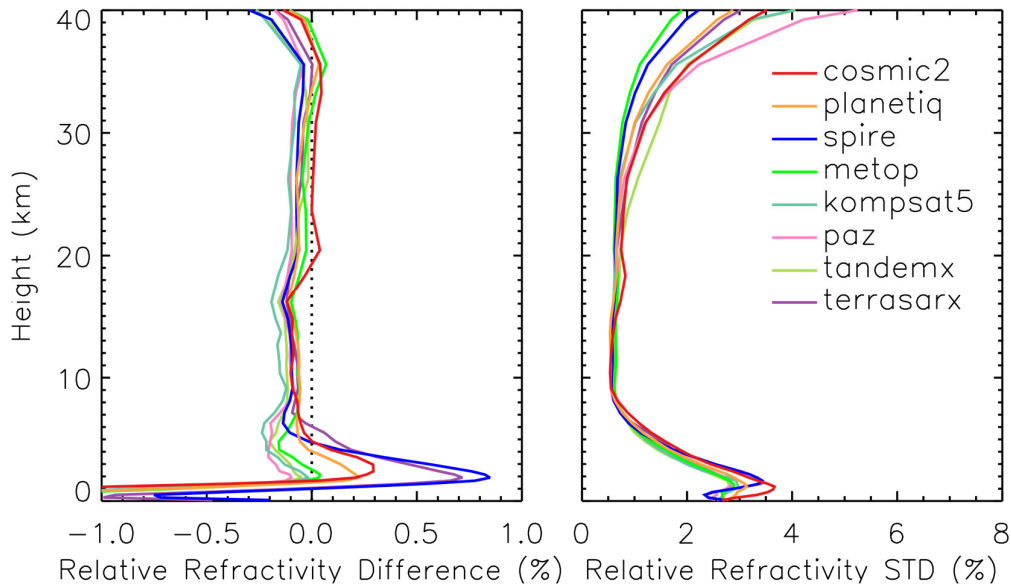


Fig. 87. Comparison of height-dependent fractional refractivity between RO observations and ERA5 simulations (O-B) among different RO missions. Refractivity mean biases (left) and standard deviations (right) in terms of fractional difference (%) for RFSI over November 2022.

In the lower troposphere (below ~ 8 km), refractivity differences exhibit a significantly larger inter-mission spread, consistent with Fig. 54, although both biases and standard deviations are

746 generally reduced. Spire and TerraSAR-X exhibit the most pronounced positive biases,
 747 reaching ~ 0.7 - 0.8% near 2 km, along with elevated standard deviations exceeding 3%.
 748 COSMIC-2 again exhibits high variability below 5 km, with standard deviations peaking at
 749 over 3.5% near 1 km. However, its mean refractivity bias remains relatively small compared
 750 to those from Spire or TerraSAR-X, suggesting increased random error rather than systematic
 751 offset.

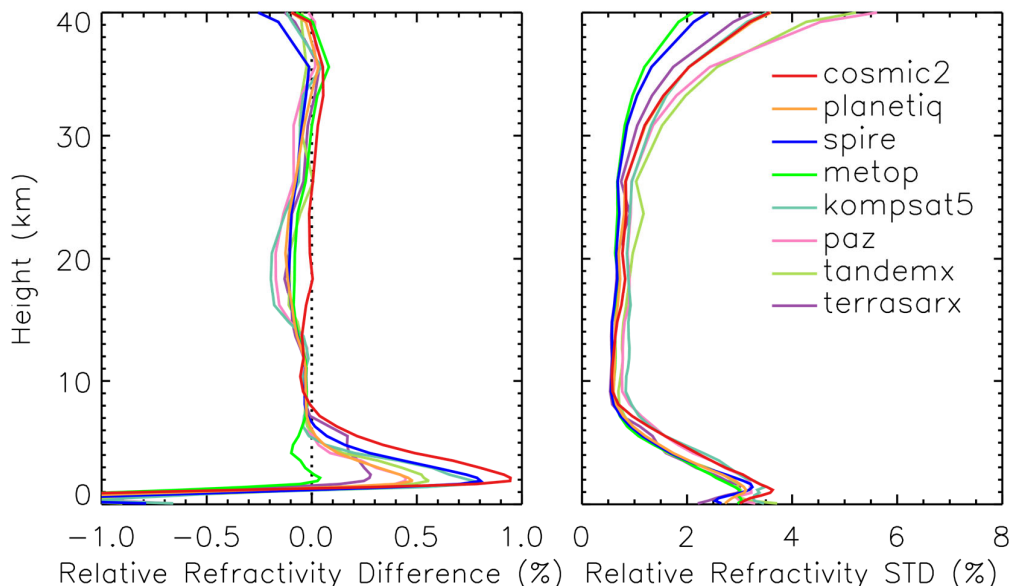
752

753 In the upper atmosphere (above ~ 35 km), where refractivity is less sensitive to the RO signal
 754 due to the exponential decrease in atmospheric density, the mean biases for all missions begin
 755 to increase negatively, reaching values of $\sim -0.2\%$ to -0.4% near 40 km. Standard deviations
 756 also rise, ranging from $\sim 2\%$ to 5%, consistent with the increased variability observed in the
 757 bending angle differences shown in Fig. 54. These errors are primarily attributed to residual
 758 ionospheric correction uncertainties and the influence of high-altitude extrapolation
 759 assumptions in the RFSI algorithm. The use of climatological models in the upper atmosphere
 760 also introduces additional variability, as refractivity becomes more sensitive to model
 761 inaccuracies in this region.

762

763 Figure 98 shows the refractivity O-B differences derived from RO data processed with the
 764 ROPP CT2 method. Between 8 and 15 km, CT2 results exhibit improved inter-mission
 765 consistency in mean bias compared to RFSI, although the standard deviations are generally
 766 larger. In the lower troposphere (below ~ 8 km), CT2 retrievals produce larger positive biases,
 767 typically around 0.5-1% near 2 km (except for Metop-B, Metop-C, and TerraSAR-X), with the
 768 largest bias observed for COSMIC-2 ($\sim 1\%$). These biases are notably larger than those from
 769 RFSI, which remain below 0.3% for most missions, except for Spire and TerraSAR-X.
 770 Between 15-25 km, the CT2 results show a greater inter-mission spread in both mean bias and
 771 standard deviation compared to RFSI. Above 25 km, CT2 and RFSI show broadly similar
 772 behavior, with rising uncertainty consistent with bending angle trends. Note that both RFSI
 773 and CT2 used geometric optics method above 25 km.

774



775

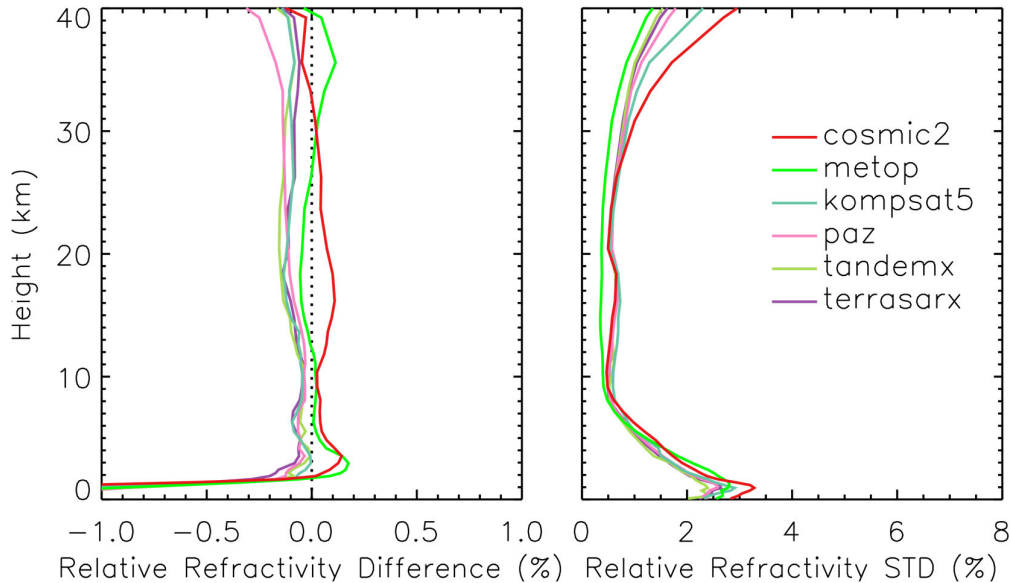
776

777

778

Fig. 98. Same as Fig. 87, but for RO refractivity processed using the ROPP package with the CT2 method.

779 Figure 109 presents the refractivity O-B differences from the EUMETSAT dataset. Note that
 780 refractivity profiles are not available for PlanetiQ and Spire in this dataset. Similar to bending
 781 angle results, COSMIC-2 exhibits a distinct positive bias in the 4-30 km region, along with a
 782 notably larger inter-missions spread in the 8-40 km range compared to CT2 (Fig. 98) and RFSI
 783 (Fig. 87) results. In contrast, in the lower troposphere (below ~8 km), the EUMETSAT
 784 retrievals show the smallest near-surface mean biases, generally within $\pm 0.2\%$ above 2.5 km,
 785 and the lowest standard deviation across all available missions. These results suggest that the
 786 refractivity data from EUMETSAT are particularly effective at mitigating noise and multipath
 787 effects near the surface.
 788



789
 790 Fig. 109. Same as Fig. 87, but for RO data provided from EUMETSAT. Note that refractivity
 791 data is not available in the EUMETSAT dataset for PlanetiQ and Spire.
 792

793 Taken together, the comparisons between Figs. 54 and 87, Figs. 65 and 98, and Figs. 76 and
 794 109 reveal that many mission-specific features observed in bending angle retrievals persist in
 795 the refractivity domain. This reinforces the importance of bending angle quality, particularly
 796 near the surface and in the upper atmosphere, for achieving accurate refractivity retrievals. The
 797 heightened sensitivity of refractivity to small-scale errors at the profile boundaries also
 798 underscores the need for robust quality control, optimized signal tracking, and careful
 799 algorithm design in future RO missions and processing systems.
 800

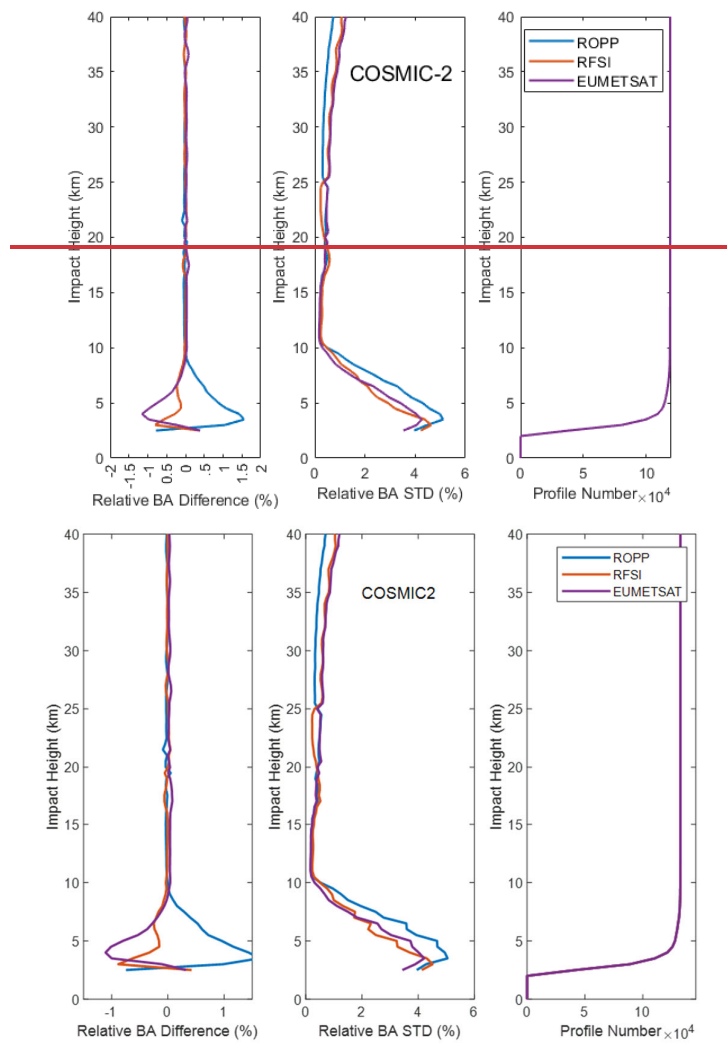
801 4.3 Structural Uncertainty among Different Processing Methods

802
 803 Figures 110-154 illustrate the structural bending angle uncertainty associated with the ROPP
 804 (CT2), RFSI, and EUMETSAT processing algorithms for five representative GNSS RO
 805 missions: COSMIC-2, Spire, PlanetiQ, Metop-B, and Metop-C. For each mission, the figure
 806 shows the height-dependent relative mean differences and standard deviations of bending
 807 angles with respect to the three-dataset mean, along with the number of common profiles
 808 processed for each algorithm.
 809

810 Several important structural differences emerge from these comparisons:
 811

812 For COSMIC-2 (Fig. 140), the three processing methods demonstrate strong consistency in the
 813 middle and upper troposphere and stratosphere (above ~ 10 km), where both the relative
 814 differences and standard deviations of bending angles remain below approximately 0.1% and
 815 1%, respectively, indicating minimal structural uncertainty. Below 10 km, method-dependent
 816 differences become more pronounced. The largest deviations are observed near the surface,
 817 with relative differences of approximately 1.5% for ROPP, -1.0% for EUMETSAT, and -0.5%
 818 for RFSI. Additionally, the ROPP algorithm exhibits higher bending angle standard deviations
 819 in the lowest 10 km, indicating greater sensitivity to retrieval ambiguities under conditions of
 820 multipath propagation. In contrast, above 25 km, ROPP shows slightly lower standard
 821 deviations than RFSI and EUMETSAT. Despite these lower-tropospheric differences, the
 822 overall structural agreement among the three COSMIC-2 processing methods is robust.
 823 Although the number of available profiles (right panel) decreases significantly near the surface,
 824 sufficient observations are present throughout the vertical domain to enable meaningful
 825 statistical comparisons.

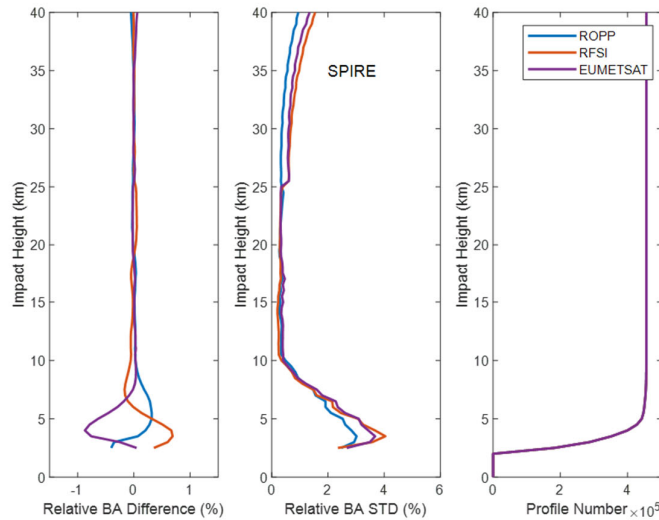
826



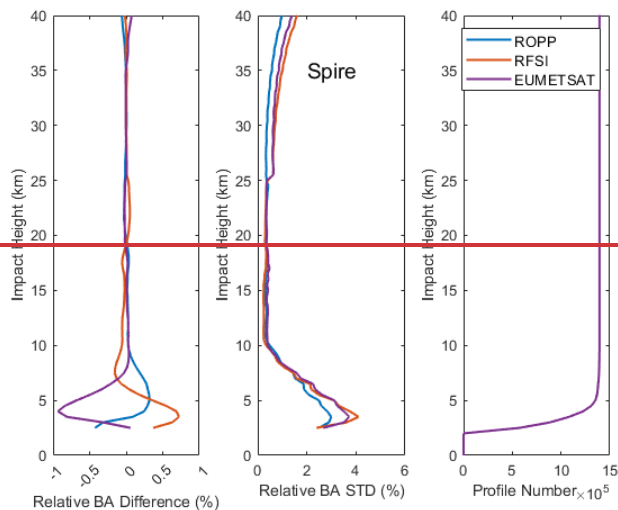
827

828 Fig. 140. Structural bending angle uncertainty among different processing methods for
 829 COSMIC-2. Note that the bending angle profiles from the EUMETSAT dataset are processed
 830 by the UCAR CDAAC using the phase-matching method.

831 For Spire (Fig. 121), a similar pattern of agreement is observed. Above approximately 10 km,
 832 the relative bending angle differences across the three methods are generally within $\pm 0.1\%$,
 833 and the standard deviations remain below 1% up to approximately 35 km, indicating good
 834 consistency in the upper atmosphere. However, RFSI exhibits a distinct pattern in the 8-25 km
 835 range, with a relative positive difference in the 19-25 km region and a negative difference in
 836 the 8-19 km region, compared to the nearly identical ROPP and EUMETSAT solutions. As
 837 with COSMIC-2, larger discrepancies emerge below 10 km. Notably, the ROPP and RFSI
 838 solutions show small positive differences near the surface (up to $\sim 0.7\%$ and $\sim 0.3\%$,
 839 respectively), whereas the EUMETSAT solution exhibits a negative deviation of up to -1.0% .
 840 The bending angle standard deviations in the lower troposphere are higher for RFSI and
 841 EUMETSAT, reaching $\sim 4\%$, while ROPP shows slightly lower variability (below 3%) near
 842 the surface. Above 25 km, ROPP again yields lower standard deviations compared to the other
 843 two methods, consistent with the COSMIC-2 results.



844



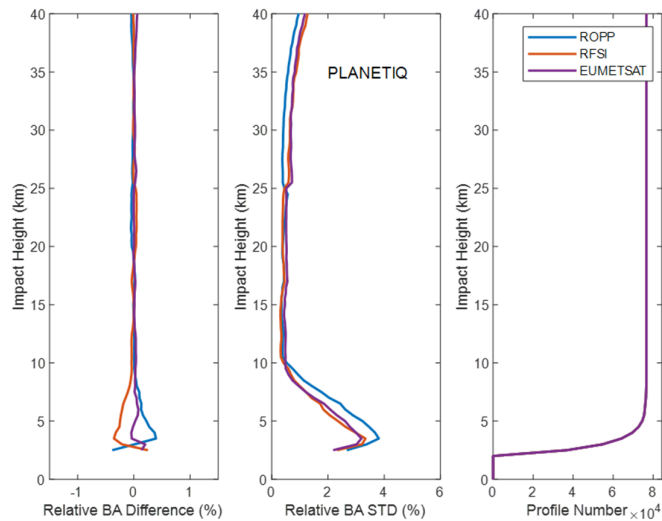
845

846 Fig. 121. Same as Fig. 140, but for Spire.

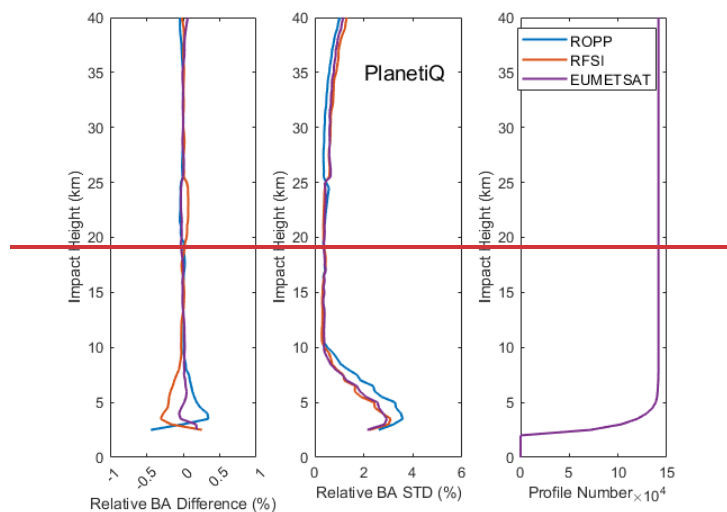
847

848 For PlanetiQ (Fig. 132), a higher level of consistency is observed among the three processing
 849 methods across the vertical profile compared to those from COSMIC-2 and Spire. Above
 850 ~ 10 km, the solutions are nearly identical, except for a slight positive deviation in the 19-25 km
 851 region from the RFSI solution. Relative bending angle differences remain within $\pm 0.05\%$, and

852 standard deviations are below 1% up to ~38 km, indicating excellent agreement in the middle
 853 and upper atmosphere. Below 10 km, small but systematic differences become evident. The
 854 ROPP solution shows a modest positive bias, peaking at approximately +0.4% near a 3 km
 855 impact height, while the RFSI solution exhibits a slight negative bias of similar magnitude.
 856 The EUMETSAT data remain close to zero throughout this region. As with COSMIC-2, the
 857 standard deviations increase toward the surface, with ROPP exhibiting greater variability
 858 below 10 km than RFSI and EUMETSAT. However, for PlanetiQ, the overall variability is
 859 lower, reaching a standard deviation of ~3% near the surface. This improved consistency
 860 suggests enhanced robustness in PlanetiQ's onboard processing, a more stable tracking
 861 geometry and antenna design, and higher SNR, which may reduce sensitivity to differences
 862 among retrieval algorithms.



863



864

865 Fig. 132. Same as Fig. 140, but for PlanetiQ.

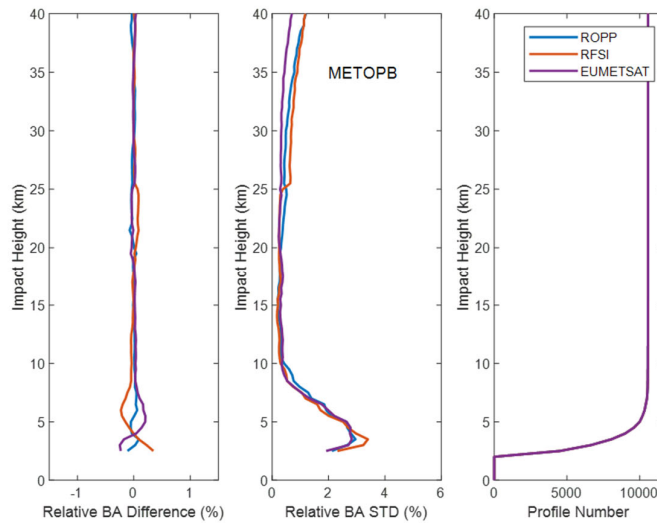
866

867 Metop-B (Fig. 143) and Metop-C (Fig. 154), both long-operational polar-orbiting satellites
 868 with mature and well-characterized instrumentation, exhibit nearly identical inter-method
 869 structural uncertainties. For brevity, the discussion here focuses on Metop-B. ~~While broad~~
 870 ~~similarities exist across the three processing methods, structural differences are more~~
 871 ~~pronounced for Metop-B than for the highly consistent PlanetiQ results.~~ Below an impact
 872 height of ~8 km, the standard deviation profiles from all three algorithms converge closely,

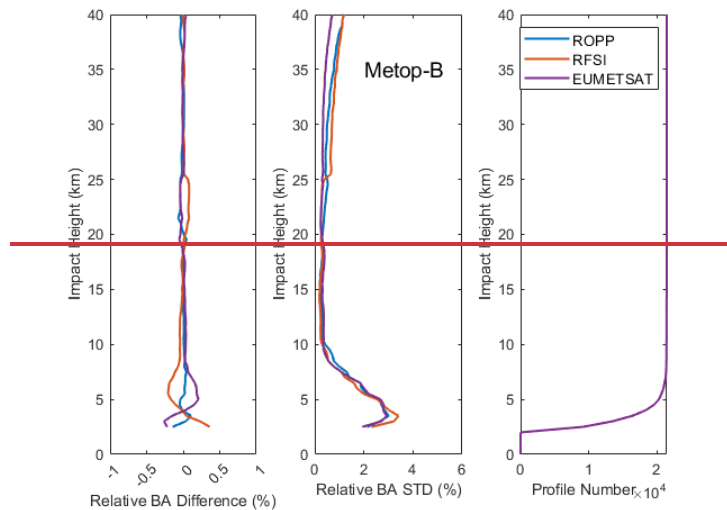
873 indicating similar variability near the surface. Relative bending angle differences show a
 874 maximum positive deviation of approximately +0.2% for the EUMETSAT solution and a
 875 negative deviation of about -0.2 % for RFSI near 5 km.

876

877 In contrast, the ROPP solution remains close to zero. A slight negative bias is also observed in
 878 the RFSI solution below ~13 km (~-0.1%). In the upper stratosphere, above 25 km, a clear
 879 separation in variability emerges: RFSI exhibits the largest standard deviations, followed by
 880 ROPP, with EUMETSAT showing the lowest variability. This divergence in STD differences
 881 near 25 km for Metop-B/C, compared to COSMIC-2, PlanetiQ, and Spire, suggests that the
 882 upper-atmospheric retrievals for Metop-B/C are more sensitive to processing methodology ~~in~~
 883 the case of Metop-B. This is supported by the data showing that in the upper stratosphere
 884 (above 25 km), the EUMETSAT algorithm exhibits the lowest variability. Given that Metop-
 885 B/C are EUMETSAT missions and their data are routinely processed by EUMETSAT, this
 886 superior performance suggests that the EUMETSAT processing methodology is likely fine-
 887 tuned and highly stable for their mature sensor platforms, enabling effective mitigation of noise
 888 and uncertainties at high altitudes, and resulting in the lowest variability observed across all
 889 datasets.



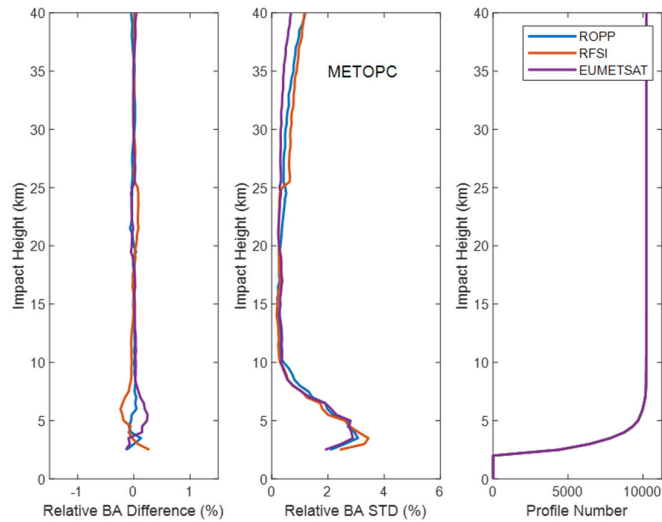
890



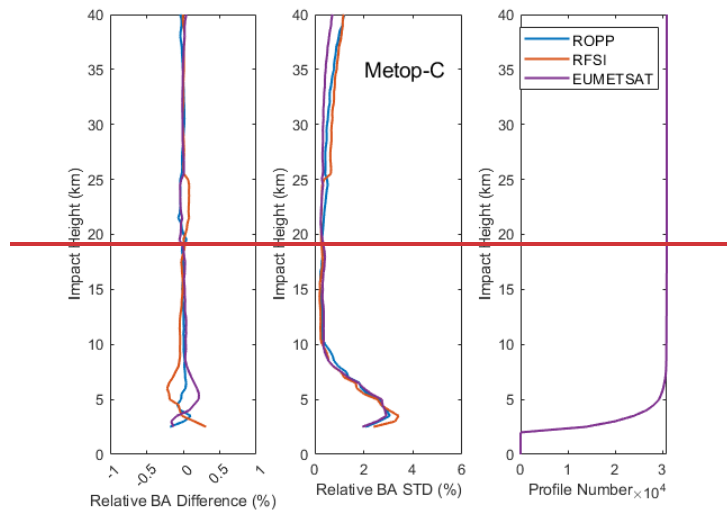
891

892 Fig. 143. Same as Fig. 140, but for Metop-B.

893



894



895

896 Fig. 154. Same as Fig. 140, but for Metop-C.

897

898 Except for COSMIC-2, RFSI shows a small positive bias ($<0.1\%$) at 20–25 km for Spire,
 899 PlanetiQ, and Metop-B/C relative to STAR ROPP and EUMETSAT. Possible causes include
 900 spectral windowing and filtering choices, as RFSI applies a sliding polynomial filter below 25
 901 km and an optimal estimation filter above 25 km, which can potentially introduceing systematic
 902 offsets. Degraded L2 signals and reduced GNSS SNR at ~ 20 -25 km further amplify noise, and
 903 because FSI is more noise-sensitive than geometric optics or canonical transform methods,
 904 incomplete noise suppression may yield small positive biases. The exact causes are under
 905 active investigation to further mitigate this effect.

906

907 These results highlight that structural uncertainty is both algorithm- and mission-dependent,
 908 influenced by signal quality, onboard processing, antenna design, and orbit characteristics. The
 909 findings highlight the crucial role of processing methodology in ensuring consistency and
 910 accuracy in retrieving RO bending angle data, particularly when data from diverse missions
 911 are used in operational weather forecasting systems. Future efforts in GNSS RO should focus
 912 on developing harmonized processing standards and conducting inter-comparison studies to
 913 quantify and mitigate structural uncertainty in bending angle datasets.

914

915 5. Discussions and Summary

916

917 This study presents the first comprehensive cross-mission intercomparison of the STAR-
918 developed Full Spectrum Inversion algorithm with the community-standard ROPP CT2 and
919 EUMETSAT dataset within the framework of ROMEX. Using bending angle and refractivity
920 profiles from key GNSS RO missions (e.g., COSMIC-2, Spire, PlanetiQ, Metop-B/C) during
921 the ROMEX period (September–November 2022), we assessed inter-algorithm consistency
922 against ERA5 reanalysis and structural uncertainty against the three-dataset mean.

923

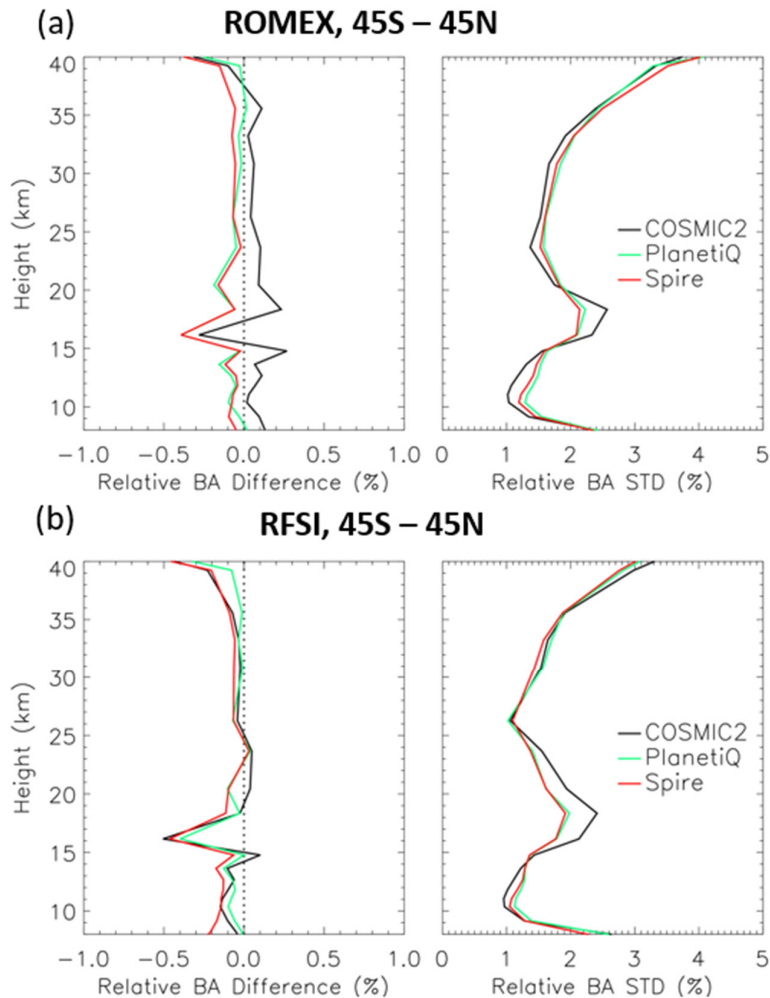
924 A significant finding is the excellent agreement among all three processing methods in the
925 middle and upper troposphere and lower stratosphere (8–35 km). In this region, the mean
926 bending angle differences remained within $\pm 0.2\%$ and the standard deviations were below 3%,
927 demonstrating the maturity and robust internal coherence of RO observations across diverse
928 missions. Similarly, refractivity retrievals in this core region exhibited high stability, with mean
929 biases within $\pm 0.15\%$ and standard deviations typically below 1%.

930

931 Anthes et al. (2025) reported that the UCAR-processed COSMIC-2 bending angles included
932 in ROMEX exhibit a positive bias of approximately 0.1–0.15% relative to ERA5 in the lower
933 stratosphere, larger than the biases seen for Spire and other ROMEX datasets. Similar lower-
934 stratospheric positive biases for UCAR COSMIC-2 have also been documented by Ho et al.
935 (2024, 2025). This difference is predominantly a representativeness effect associated with
936 orbit-dependent sampling over a non-spherical Earth (the azimuth effect), rather than a true
937 systematic bias, and therefore does not significantly impact data assimilation. The remaining
938 small component (less than 0.05%) is attributed to the sideways displacement of the occultation
939 plane and can be mitigated by impact height correction during RO processing (Anthes et al.,
940 2025). Figure 165 provides a zoomed-in comparison of the height-dependent fractional O–B
941 bending-angle differences for the COSMIC-2, Spire, and PlanetiQ missions, between the
942 EUMETSAT/UCAR processing and the STAR RFSI processing. In Fig. 165a, the COSMIC-
943 2 data are from UCAR, while the Spire and PlanetiQ datasets are processed by EUMETSAT;
944 in Fig. 165b, all three missions are processed consistently by STAR RFSI.

945

946 While the UCAR-provided COSMIC-2 ROMEX datasets show a small positive O-B bias
947 compared to EUMETSAT-processed Spire and PlanetiQ data in the lower stratosphere (Fig.
948 165a), the STAR RFSI-processed COSMIC-2 bending angles exhibit improved consistency
949 with the Spire and PlanetiQ results (Fig. 165b). One contributing factor may be the treatment
950 of horizontal tangent-point sliding within the RFSI framework. While a consistent occultation
951 point definition is applied across missions in this study, differences in occultation point
952 definitions (or georeferencing) among processing centers can affect the magnitude of the
953 sliding-related correction. As noted in Anthes et al. (2025), UCAR defines the occultation point
954 as the location where the L1 excess phase exceeds 500 m, typically in the lower troposphere.
955 In contrast, **ROPPRFSI** defines it as the location where the straight-line tangent altitude equals
956 zero, typically in the upper troposphere–lower stratosphere (UTLS). This sideways sliding
957 effect can introduce a positive bias in COSMIC-2 bending angles of up to $\sim 0.05\%$. The
958 underlying cause of the subtle differences in the lower-stratospheric O–B bending-angle among
959 the processing centers (STAR, EUMETSAT, UCAR) will be examined further in future work.



960
 961 Fig. 165. Zoomed-in height-dependent fractional bending-angle differences (O-B) between
 962 RO observations and ERA5 simulations are shown for COSMIC-2, Spire, and PlanetiQ. Panels
 963 (a) and (b) display the mean bending-angle biases (left) and standard deviations (right) for RO
 964 data processed by EUMETSAT and by STAR RFSI, respectively.

965
 966 Conversely, larger discrepancies and heightened variability emerged in the lower troposphere
 967 (below ~ 8 km) and upper atmosphere (above ~ 35 km). These regions are challenged by
 968 multipath effects, increased tracking noise, and varying SNR. The FSI method, designed to
 969 resolve fine-scale atmospheric structures by leveraging full-spectrum signal information,
 970 demonstrated improved sensitivity in the lower atmosphere (Adhikari et al., 2021), particularly
 971 for missions such as PlanetiQ and Metop-B/C. However, it also showed increased variability
 972 and greater dependence on SNR cut-off and quality control thresholds, as seen with Spire and
 973 TerraSAR-X near the surface. In contrast, the CT2 method, while generally yielding smoother
 974 profiles with reduced noise, sometimes showed larger near-surface biases (e.g., CT2 for
 975 COSMIC-2 and Spire), suggesting a more conservative approach that might underestimate
 976 bending in complex conditions. EUMETSAT's dataset, in particular, achieved the smallest
 977 near-surface bending angle and refractivity biases across missions, indicating effective
 978 mitigation of noise and multipath.

979
 980 A crucial finding of this study is that structural uncertainty depends on both the processing
 981 algorithm and the satellite mission. A greater inter-method spread was observed across all

982 missions below 8 km, likely due to their distinct approaches to handling multipath, noise, and
983 signal truncation. This structural uncertainty complicates the consistent use of multi-mission
984 RO data. For instance, COSMIC-2 data processed by ROPP CT2 showed higher near-surface
985 variability than those processed by RFSI and EUMETSAT. In contrast, missions like Metop-
986 B/C exhibited stronger consistency across all three methods, while PlanetiQ demonstrated the
987 highest inter-method consistency throughout the profile. These mission-specific patterns,
988 clearly illustrated in Figs. 140-154, underscore the critical need to characterize and account for
989 algorithmic effects when assimilating multi-mission RO data into operational weather
990 forecasting systems. The explicit comparison of the total O-B standard deviation (Figs. 54-76)
991 with the structural uncertainty (Figs. 140-154) quantifies the contribution of retrieval algorithm
992 differences to the total error budget, demonstrating that structural differences account for
993 approximately one-fourth of the total O-B standard deviation over all the altitudes, providing
994 a critical metric for interpreting ROMEX forecast impact studies and refining GNSS RO data
995 assimilation systems.

996
997 The ROMEX results unequivocally highlight the importance of quantifying algorithm-related
998 structural uncertainty for data assimilation applications. To ensure a consistent and optimal
999 representation of RO data in numerical weather prediction systems, it may be necessary to
1000 harmonize retrieval strategies across different processing centers or to apply mission- and
1001 algorithm-specific bias corrections.

1002
1003 The successful integration of STAR's FSI algorithm into ROPP version 10.0 represents a
1004 significant advancement, providing users with a robust and flexible alternative to existing
1005 algorithms. This enhancement facilitates consistent RO data processing across both
1006 government-funded and commercial missions, offering customizable settings to meet specific
1007 scientific and operational requirements.

1008
1009 In summary, this study demonstrates the critical influence of algorithm choice, particularly in
1010 the lower troposphere; confirms strong consistency among processors in the mid-to-upper
1011 atmosphere; identifies distinct mission-dependent structural uncertainties; and recommends
1012 applying bias correction or ensemble strategies to improve data assimilation. The findings
1013 strongly support continued efforts to harmonize across agencies through collaborative
1014 initiatives, such as ROMEX. As the volume and diversity of GNSS RO data continue to
1015 expand, these insights underscore the paramount need for robust algorithm development,
1016 thorough uncertainty quantification, and coordinated processing strategies to fully leverage RO
1017 observations and advance weather forecasting and climate monitoring capabilities.

1018
1019 **Code/Data availability.** The ROMEX data processed by EUMETSAT are available free of
1020 charge through ROM SAF, subject to the ROMEX terms and conditions. Further information
1021 is available at <https://rowg.org/ro-modeling-experiment-romex/> (last access: 28 March 2026).
1022 The ROMEX data processed by NOAA/STAR are available from STAR under the ROMEX
1023 terms and conditions. ERA5 data are available from the ECMWF data catalogue at
1024 <https://www.ecmwf.int/en/forecasts/datasets/browse-reanalysis-datasets> (last access: 28
1025 March 2026).

1026
1027 **Author contribution.** YC developed the RO processing system and designed the research
1028 plan, supervised the study, and prepared the manuscript. XZ conducted the data processing and
1029 prepared the figures and analysis. XJ contributed to the preparation of the data analysis and
1030 figures. SH provided overall scientific guidance throughout the project. XS and TL led the

1031 theoretical development and conducted testing to improve the results. All co-authors
1032 contributed to the interpretation of the results and to the writing and revision of the manuscript.

1033

1034 **Competing interests.** The contact author has declared that none of the authors has any
1035 competing interests.

1036

1037 **Disclaimer. Publisher's note:** Copernicus Publications remains neutral with regard to
1038 jurisdictional claims made in the text, published maps, institutional affiliations, or any other
1039 geographical representation in this paper. While Copernicus Publications makes every effort
1040 to include appropriate place names, the final responsibility lies with the authors. Views
1041 expressed in the text are those of the authors and do not necessarily reflect the views of the
1042 publisher.

1043

1044 **Special issue statement.** This article is part of the special issue “The Radio Occultation
1045 Modeling EXperiment (ROMEX): observational quality, processing, and numerical weather
1046 prediction (NWP) applications”. It is not associated with a conference.

1047

1048 **Acknowledgments**

1049 This research received no external funding and was supported by the NOAA Center for
1050 Satellite Applications and Research (STAR). We thank the ROMEX coordination team and the
1051 ROM SAF for facilitating access to the processed datasets. This work was further supported
1052 by the NOAA/NESDIS/STAR Product Development Readiness and Applications (PDRA)
1053 fund and by NOAA grants NA19NES4320002 and NA24NESX432C0001 (Cooperative
1054 Institute for Satellite Earth System Studies-CISESS) at the University of Maryland/ESSIC. The
1055 authors also thank Dr. Loknath Adhikari for his contributions to the development of the FSI
1056 algorithm, Josep Aparicio and two anonymous reviewers for their constructive suggestions,
1057 which have helped improve the quality and clarity of this manuscript. The scientific results and
1058 conclusions, as well as any views or opinions expressed herein, are those of the author(s) and
1059 do not necessarily reflect those of NOAA or the Department of Commerce.

1060

1061 **References**

1062 Adhikari, A., Xie, F., and Haase, J. S.: Application of the full spectrum inversion algorithm to
1063 simulated airborne GPS radio occultation signals, *Atmos. Meas. Tech.*, 9, 5077–5086,
1064 <https://doi.org/10.5194/amt-9-5077-2016>, 2016.

1065

1066 Adhikari, A., Ho, S.-P., and Zhou, X.: Inverting COSMIC-2 phase data to bending angle and
1067 refractivity using the Full Spectrum Inversion method, *Remote Sens.*, 13, 1793,
1068 <https://doi.org/10.3390/rs13091793>, 2021.

1069

1070 Anthes, R. A.: Exploring Earth's atmosphere with radio occultation: Contributions to weather,
1071 climate, and space weather, *Atmos. Meas. Tech.*, 4, 1077–1103, [https://doi.org/10.5194/amt-](https://doi.org/10.5194/amt-4-1077-2011)
1072 [4-1077-2011](https://doi.org/10.5194/amt-4-1077-2011), 2011.

1073

1074 Anthes, R. A., Bernhardt, P. A., Chen, Y., Cucurull, L., Dymond, K. F., Ector, D., Healy, S.
1075 B., Ho, S.-P., Hunt, D. C., Kuo, Y.-H., and others: The COSMIC/FORMOSAT-3 Mission:
1076 Early Results, *Bull. Amer. Meteor. Soc.*, 89, 313–334, [https://doi.org/10.1175/BAMS-89-3-](https://doi.org/10.1175/BAMS-89-3-313)
1077 [313](https://doi.org/10.1175/BAMS-89-3-313), 2008.

1078

1079 Anthes, R. A., Marquardt, C., Ruston, B., and Shao, H.: Radio Occultation Modeling
1080 Experiment (ROMEX): Determining the impact of radio occultation observations on numerical
1081 weather prediction, *Bull. Amer. Meteor. Soc.*, 105, E1552–E1568,
1082 <https://doi.org/10.1175/BAMS-D-23-0326.1>, 2024.
1083
1084 Anthes, R., Sjoberg, J., Starr, J., and Zeng, Z.: Evaluation of biases and uncertainties in
1085 ROMEX radio occultation observations, *Atmos. Meas. Tech.*, 18, 6997–7019,
1086 <https://doi.org/10.5194/amt-18-6997-2025>, 2025.
1087
1088 Born, M. and Wolf, E.: *Principles of Optics*, Cambridge University Press, New York, 1999.
1089
1090 Chen, Y., Zhou, X., Ho, S.-P., Shao, X., and Liu, T.-C.: Comparison of Radio Occultation
1091 Bending Angle and Refractivity Processed by Different Inversion Algorithms from Multi-RO
1092 Missions, in: *IGARSS 2024 IEEE Int. Geosci. Remote Sens. Symp.*, Athens, Greece, 2024,
1093 8904–8907, <https://doi.org/10.1109/IGARSS53475.2024.10641034>, 2024.
1094
1095 Cucurull, L., Derber, J. C., Treadon, R., and Purser, R. J.: Assimilation of global positioning
1096 system radio occultation observations into NCEP’s Global Data Assimilation System, *Mon.*
1097 *Weather Rev.*, 135, 3174–3193, <https://doi.org/10.1175/MWR3461.1>, 2007.
1098
1099 Fjeldbo, G. F., Kliore, A. J., and Eshelman, V. R.: The neutral atmosphere of Venus as studied
1100 with the Mariner V radio occultation experiments, *J. Astro.*, 76, 123–140, 1971. Gorbunov, M.,
1101 Irisov, V., and Rocken, C.: The Influence of the Signal-to-Noise Ratio upon Radio Occultation
1102 Retrievals, *Remote Sens.*, 14, 2742, <https://doi.org/10.3390/rs14122742>, 2022a.
1103
1104 Gorbunov, M., Irisov, V., and Rocken, C.: Noise Floor and Signal-to-Noise Ratio of Radio
1105 Occultation Observations: A Cross-Mission Statistical Comparison, *Remote Sens.*, 14, 691,
1106 <https://doi.org/10.3390/rs14030691>, 2022b.
1107
1108 Gorbunov, M. E.: Radioholographic analysis of radio occultation data in multipath zones,
1109 *Radio Sci.*, 37, 1008, <https://doi.org/10.1029/2000RS002577>, 2002a.
1110
1111 Gorbunov, M. E.: Canonical transform method for processing radio occultation data in the
1112 lower troposphere, *Radio Sci.*, 37, 1076, <https://doi.org/10.1029/2000RS002592>, 2002b.
1113
1114 Gorbunov, M. E.: Ionospheric correction and statistical optimization of radio occultation data,
1115 *Radio Sci.*, 37, <https://doi.org/10.1029/2000RS002370>, 2002c.
1116
1117 Gorbunov, M. E., Lauritsen, K. B., Rhodin, A., Tomassini, M., and Kornblueh, L.: Analysis of
1118 the CHAMP experimental data on radio-occultation sounding of the Earth’s atmosphere, *Izv.*
1119 *Atmos. Ocean. Phys.*, 41, 798–813, 2005.
1120
1121 Hajj, G. A., Kursinski, E. R., Romans, L. J., Bertiger, W. I., and Leroy, S. S.: A technical
1122 description of atmospheric sounding by GPS occultation, *J. Atmos. Sol.-Terr. Phys.*, 64, 451–
1123 469, [https://doi.org/10.1016/S1364-6826\(01\)00114-6](https://doi.org/10.1016/S1364-6826(01)00114-6), 2002.
1124
1125 Healy, S. B.: Forecast impact experiment with a constellation of GPS radio occultation
1126 receivers, *Atmos. Sci. Lett.*, 9, 111–118, <https://doi.org/10.1002/asl.169>, 2008.
1127

1128 Hersbach, H., Bell, B., Berrisford, P., Biavati, G., Horányi, A., Muñoz Sabater, J., Nicolas, J.,
1129 Peubey, C., Radu, R., Rozum, I., Schepers, D., Simmons, A., Soci, C., Dee, D., and Thépaut,
1130 J.-N.: ERA5 hourly data on pressure levels from 1940 to present, Copernicus Climate Change
1131 Service (C3S) Climate Data Store (CDS) [data set], <https://doi.org/10.24381/cds.bd0915c6>,
1132 accessed: 6 August 2024.

1133

1134 Hedin, A. E., Extension of the MSIS thermosphere model into the middle and lower
1135 atmosphere, *J. Geophys. Res.*, 96, 1159–1172, 1991.

1136

1137 [Liu, H., Kuo, Y.-H., Sokolovskiy, S., Zou, X., Zeng, Z., Hsiao, L.-F., and Ruston, B.: A quality](#)
1138 [control procedure based on bending angle measurement uncertainty for radio occultation data](#)
1139 [assimilation in the tropical lower troposphere, *J. Atmos. Oceanic Tech.*, 35\(10\), 2117-2131,](#)
1140 [2018, doi: 10.1075/JTECHD-17.0224.1.](#)

1141

1142 Ho, S.-P., Anthes, R. A., Ao, C. O., Healy, S., Horányi, A., Hunt, D., Mannucci, A. J.,
1143 Pedatella, N., Randel, W. J., and Simmons, A.: The COSMIC/FORMOSAT-3 Radio
1144 Occultation Mission after 12 Years: Accomplishments, Remaining Challenges, and Potential
1145 Impacts of COSMIC-2, *Bull. Amer. Meteor. Soc.*, 101, E1107–E1136,
1146 <https://doi.org/10.1175/BAMS-D-19-0027.1>, 2020.

1147

1148 Ho, S.-P., Hunt, D., Steiner, A. K., Mannucci, A. J., Kirchengast, G., Gleisner, H., Heise, S.,
1149 von Engel, A., Marquardt, C., Sokolovskiy, S., Schreiner, W., Scherllin-Pirscher, B., Ao, C.,
1150 Wickert, J., Syndergaard, S., Lauritsen, K. B., Leroy, S., Kursinski, E. R., Kuo, Y.-H.,
1151 Foelsche, U., Schmidt, T., and Gorbunov, M.: Reproducibility of GPS radio occultation data
1152 for climate monitoring: Profile-to-profile inter-comparison of CHAMP climate records 2002
1153 to 2008 from six data centers, *J. Geophys. Res.*, 117, D18111,
1154 <https://doi.org/10.1029/2012JD017665>, 2012.

1155

1156 Ho, S.-P., Zhou, X., Shao, X., Chen, Y., Jing, X., and Miller, W.: Using the Commercial GNSS
1157 RO Spire Data in the Neutral Atmosphere for Climate and Weather Prediction Studies, *Remote*
1158 *Sens.*, 15, 4836, <https://doi.org/10.3390/rs15194836>, 2023.

1159

1160 Ho, S.-P., Shao, X., Chen, Y., Zhou, J., Gu, G., Miller, W., and Jing, X.: Lessons Learned from
1161 the Preparation and Evaluation of Multiple GNSS RO Data for the ROMEX from
1162 NOAA/STAR. Presentation at the COSMIC/JCSDA Workshop and IROWG-10, Boulder,
1163 Colorado, 12-18 September 2024. Available at: [https://www.cosmic.ucar.edu/events/cosmic-](https://www.cosmic.ucar.edu/events/cosmic-jcsda-workshop-irowg-10/agenda)
1164 [jcsda-workshop-irowg-10/agenda](https://www.cosmic.ucar.edu/events/cosmic-jcsda-workshop-irowg-10/agenda), 2024.

1165

1166 Ho, S.-P., Shao, X., Chen, Y., Zhou, J., and Miller, W.: Advances in ROMEX data processing
1167 and evaluation: Lessons from NOAA STAR. Presentation at the 2nd ROMEX Workshop,
1168 February 27, 2025, at EUMETSAT, Darmstadt, Germany. Available at
1169 <https://www.eventsforce.net/romex2025>, 2025.

1170

1171 Jensen, A. S., Lohmann, M., Benzon, H.-H., and Nielsen, A. S.: Full spectrum inversion of
1172 radio occultation signals, *Radio Sci.*, 38, 1040, <https://doi.org/10.1029/2002RS002763>, 2003.

1173

1174 Jensen, A. S., Lohmann, M., Nielsen, A. S., and Benzon, H.-H.: Geometrical optics phase
1175 matching of radio occultation signals, *Radio Sci.*, 39, RS3009,
1176 <https://doi.org/10.1029/2003RS002899>, 2004.

1177

1178 Kursinski, E. R., Hajj, G. A., Schofield, J. T., Linfield, R. P., and Hardy, K. R.: Observing
1179 Earth's atmosphere with radio occultation measurements using the Global Positioning System,
1180 *J. Geophys. Res.*, 102, 23429–23465, <https://doi.org/10.1029/97JD01569>, 1997.
1181

1182 Luzum, B. and Petit, G.: The IERS conventions (2010): Reference systems and new models,
1183 *Proc. Int. Astron. Union*, 10, 227–228, 2012.
1184

1185 Miller, W., Chen, Y., Ho, S.-P., and Shao, X.: Exploring the Value of Spire GNSS Radio
1186 Occultation Bending Angle Assimilation for Improving HWRF Model Forecasts of Atlantic
1187 Hurricane Intensity, *Weather and Forecasting*, 40 (6), 809-827, <https://doi.org/10.1175/waf-d-24-0092.1>, 2025.
1188

1189 Paoella, S., et al. (2025). Assessment of operational non-time-critical Sentinel-6A Michael
1191 Freilich radio occultation data: insights into tropospheric GNSS signal cut-off strategies and
1192 processor improvements. *Atmos. Meas. Tech.*, 18, 2825–2845. <https://doi.org/10.5194/amt-18-2825-2025>
1193
1194

1195 Petit, G. and Luzum, B. (Eds.): IERS Technical Note No. 36, IERS, Frankfurt am Main, 2010,
1196 available at: <https://apps.dtic.mil/sti/citations/ADA535671> (last access: 6 August 2024).
1197

1198 Rocken, C., Anthes, R., Exner, M., Hunt, D., Sokolovskiy, S., Ware, R., Gorbunov, M.,
1199 Schreiner, W., Feng, D., Herman, B., Kuo, Y.-H., and Zou, X.: Analysis and validation of
1200 GPS/MET data in the neutral atmosphere, *J. Geophys. Res.-Atmos.*, 102, 29849–29866,
1201 <https://doi.org/10.1029/97JD02400>, 1997.
1202

1203 Schreiner, W. S., Weiss, J. P., Anthes, R. A., Braun, J., Chu, V., Fong, J., Hunt, D., Kuo, Y.-
1204 H., Meehan, T., Serafino, W., Sjoberg, J., Sokolovskiy, S., Talaat, E., Wee, T. K., and Zeng,
1205 Z.: COSMIC-2 radio occultation constellation: First results, *Geophys. Res. Lett.*, 47,
1206 e2019GL086841, <https://doi.org/10.1029/2019GL086841>, 2020.
1207

1208 Shao, H., and Folsche, U.: ROMEX: Status and First Lessons Learned, Presentation at IROWG
1209 CGMS-52 Plenary, 2024, Washington, DC, USA. Available at <https://irowg.org/wpcms/wp-content/uploads/2025/04/CGMS-52-IROWG-WP-03.pdf>, 2024.
1210
1211

1212 Sokolovskiy, S., Rocken, C., Schreiner, W., Hunt, D., and Johnson, J.: Postprocessing of L1
1213 GPS radio occultation signals recorded in open-loop mode, *Radio Sci.*, 44, RS2002,
1214 <https://doi.org/10.1029/2008RS003907>, 2009.
1215

1216 Sokolovskiy, S., Rocken, C., Schreiner, W., and Hunt, D.: On the uncertainty of radio
1217 occultation inversions in the lower troposphere, *J. Geophys. Res.*, 115, D22111,
1218 <https://doi.org/10.1029/2010JD014058>, 2010.
1219

1220 Steiner, A. K., Lackner, B. C., Pirscher, B., Hegerl, G. C., and Foelsche, U.: The contribution
1221 of radio occultation to the assessment of tropospheric temperature trends, *J. Climate*, 24, 4936–
1222 4950, <https://doi.org/10.1175/2011JCLI3982.1>, 2011.
1223

1224 Steiner, A. K., Ladstädter, F., Ao, C. O., Gleisner, H., Ho, S.-P., Hunt, D., Schmidt, T.,
1225 Foelsche, U., Kirchengast, G., Kuo, Y.-H., and others: Consistency and structural uncertainty
1226 of multi-mission GPS radio occultation records, *Atmos. Meas. Tech.*, 13, 2547–2575,
1227 <https://doi.org/10.5194/amt-13-2547-2020>, 2020.

- 1228
1229 The Radio Occultation Processing Package (ROPP) Pre-processor Module User Guide, version
1230 10.0, ROM SAF Consortium, Ref: SAF/ROM/METO/UG/ROPP/004, 30 September 2020.
1231
1232 Vorob'ev, V. V. and Krasil'nikova, T. G., Estimation of the accuracy of the atmospheric
1233 refractive index recovery from Doppler shift measurements at frequencies used in the
1234 NAVSTAR system, *USSR Phys. Atmos. Ocean, Engl. Transl.*, 29, 602–609, 1994.